Distinct functions of parvalbumin and somatostatin interneurons in the anterior cingulate cortex result in heterogeneity of social interaction impairments

Shengxi Wu (shengxi@fmmu.edu.cn)
Fourth Military Medical University https://orcid.org/0000-0002-3210-9567
Chuchu Qi
Fourth Military Medical University
Wenqi Sima
Fourth Military Medical University
Honghui Miao
Fourth Military Medical University
Erling Hu
Fourth Military Medical University
Junye Ge
Fourth Military Medical University
Mao Deng
Chinese Academy of Sciences https://orcid.org/0009-0003-7633-5915
Andi Chen
Guangdong Institute of Intelligence Science and Technology
Weiyi Ye
Chinese Academy of Sciences
Qian Xue
Wenting Wang
Department of Neurobiology, School of Basic Medicine, Fourth Military Medical University
https://orcid.org/0000-0002-8344-0102
Qian Chen
Chinese Academy of Sciences

Article

Keywords: anterior cingulate cortex, parvalbumin interneuron, somatostatin interneuron, social interaction, heterogeneity, Kcnh7, autism

Posted Date: February 6th, 2024

DOI: https://doi.org/10.21203/rs.3.rs-3841366/v1

Additional Declarations: There is **NO** Competing Interest.

Distinct functions of parvalbumin and somatostatin interneurons in the anterior cingulate cortex result in heterogeneity of social interaction impairments

Chuchu Qi[1]†, Wenqi Sima[1]†, Honghui Mao[1]†, Erling Hu, Junye Ge[1], [1], Mao Deng[2], Andi Chen[3], Weiyi Ye[2], Qian Xue[1], Wenting Wang[1*], Qian Chen[2*], Shengxi Wu[1*]

[1] Department of Neurobiology, School of Basic Medicine, Fourth Military Medical University, Xi'an, Shaanxi 710032, China

[2] Zhongshan Institute for Drug Discovery, Shanghai Institute of Materia Medica, Chinese Academy of Sciences, Zhongshan 528400, China

[3] Guangdong Institute of Intelligence Science and Technology, Hengqin, Zhuhai, Guangdong 519031, China

† These authors contributed equally to this work.

* Corresponding authors

Shengxi Wu, Department of Neurobiology, School of Basic Medicine, Fourth Military Medical University, Xi'an 710032, China. Tel: +86-29-8471-2316; Email: shengxi@fmmu.edu.cn;

Wenting Wang, Department of Neurobiology, School of Basic Medicine, Fourth Military Medical University, Xi'an 710032, China. Tel: +86-29-8471-2316; Email: wwt0657@fmmu.edu.cn

Qian Chen, Zhongshan Institute for Drug Discovery, Shanghai Institute of Materia Medica, Chinese Academy of Sciences, Zhongshan 528400, China. Email: chenqian@zidd.ac.cn

Abstract

The anterior cingulate cortex (ACC) serves as a core region in social networks, and impairments in this area have been identified in autism spectrum disorders. Our prior research demonstrated that deficits in pyramidal neurons in ACC adversely impacted mouse social interaction. The preservation of functional output in the ACC by pyramidal neurons relies on the dynamic regulation by the different types of interneurons. However, the precise regulatory roles of distinct interneurons within the ACC in shaping social interaction have hitherto remained largely enigmatic. In this study, we elucidated the involvement of parvalbumin (PV) and somatostatin (SST) interneurons within the ACC in modulating social interaction behavior. Specifically, we ascertain that PV interneurons play a more prominent role in initiating sociability, whereas SST interneurons uniquely influence social preference. Notably, the downregulation of the autism high-risk gene *Kcnh7* is identified in both PV and SST interneurons within the *Shank3* knockout (KO) autistic mouse model. Further, the selective KO of *Kcnh7* in PV- or SST-positive neurons contributes to disruptions in sociability and social preference, respectively. The divergent modulation of social interaction by PV and SST interneurons in the ACC is attributed to the distinct input received by these neuronal subtypes. Our findings offer nuanced insights into the multifaceted roles of PV and SST neurons within the ACC in the context of social interaction, contributing to a comprehensive understanding of the neurobiological underpinnings of social behavior disorders in autism. The delineation of these mechanisms is imperative for advancing our comprehension of the etiological basis of autism, thereby paving the way for novel avenues of research aimed at addressing the heterogeneous phenotypes associated with social interaction dysfunction in cortical interneurons.

Key words: anterior cingulate cortex, parvalbumin interneuron, somatostatin interneuron, social interaction, heterogeneity, *Kcnh7*, autism

Social behavior encompasses a repertoire of critical adaptive skills for social species, including social interaction, social hierarchy, social fear, courtship behavior, and parenting behavior, all of which are important for population maintenance and offspring reproduction1. Of these, social interaction holds particular significance as it serves as a foundational precursor for other social behaviors by furnishing essential informational cues, encompassing sociability (identifying unfamiliar individuals) and preference (differentiating between unfamiliar and familiar individuals)[2-4]. Evolutionary conservation underscores the indispensability of social interaction in social life[5-8]. Investigating the neural underpinnings of social interaction using animal models not only enhances our comprehension of nervous system function and the construction of comprehensive brain functional networks but also furnishes valuable insights into the pathogenesis of related disorders, such as autism spectrum disorders (ASDs)[9, 10].

The anterior cingulate cortex (ACC), recognized for its regulatory role in cognition[11], attention[12], emotion[13, 14], decision-making[15], and somatic touch[16], is an area of particular interest concerning social interaction. ACC signaling alterations, as evidenced by imaging studies, have been associated with variations in social interests in both human and nonhuman primates[12, 17, 18]. Moreover, structural and functional alterations in the ACC correlate positively with deficits in social behavior observed in individuals with autism[19-21]. Despite its pivotal role, the ACC's contribution to social behavior has been comparatively underexplored. Our prior research establishes a significant causal link between social interaction deficits and dysfunction of pyramidal neurons in the ACC of mice with autistic-like behaviors, underscoring the critical role of these neurons in social interaction[22]. This suggests that these neurons play a critical role in social interaction.

Pyramidal neurons (PNs) are central to information transmission in the cortex, reliant upon precise regulation by surrounding GABAergic interneurons[23-25]. Parvalbumin (PV) and somatostatin (SST) interneurons, the two primary types directly innervating

pyramidal neurons in the ACC, modulate the dynamic role of pyramidal neurons and maintain stable ACC functioning by receiving projections from other brain regions[24, 26-30]. However, the specific contributions of these interneurons to social interaction, as key regulators of ACC function, remain a significant scientific question, particularly in the context of social deficits associated with ASD. There is high heterogeneity in the diverse behavioral abnormalities associated with the core symptoms of ASD[31, 32]. Sociability and social preference, which are essential components of social interaction, are disrupted in both individuals with autism and autistic animal models. Given the fact that distinct roles played by different types of interneurons in regulating the same behavior[23, 24], we hypothesize that PV-positive and SST-positive neurons may contribute differentially to the observed heterogeneity in ASD due to their distinct roles in regulating behavior.

In the present study, we found that both PV and SST interneurons in the ACC are implicated in social interaction, with PV interneurons displaying heightened sensitivity to sociability and SST interneurons exhibiting more pronounced changes during social preference. Notably, using *Shank3* mutant mice as a well-established ASD model, we identified reduced expression of the *Kcnh7* gene, also a risk gene for ASD[33], through single-cell RNA sequencing. Employing a Cre-dependent CRISPR-Cas9 viral approach to individually knockout (KO) *Kcnh7* in PV or SST neurons in the ACC, we demonstrated that PV interneuron *Kcnh7* KO led to impairments in social ability, while SST neuron *Kcnh7* KO replicated deficits in social preference. The distinctive roles of PV and SST interneurons are attributed to their divergent inputs. These findings provide direct evidence for the distinct roles of PV and SST interneurons in the ACC in social interaction and offer insights into the potential mechanisms contributing to the heterogeneity of social dysfunction in individuals with ASD.

Results

The activities of the PV and SST interneurons exhibited similar trends but

different detailed dynamics in the context of social interaction.

Our previous work has indicated that pyramidal neurons in ACC are involved in encoding signals associated with social interaction[22]. And also, distinct inhibitory effects on pyramidal neurons in the ACC have been observed for PV and SST interneurons[34]. Initially, we aim to investigate the potential involvement of the PV and SST interneurons in modulating social interaction behavior. We selectively expressed the calcium indicator GCaMP7s in PV or SST interneurons by injecting AAV2/9-FLEX-GCaMP7s into the ACC of PV-Cre or SST-Cre transgenic mice (**Fig. 1A-C, and Extended Data Fig. 1**). Subsequently, we quantitatively measured changes in calcium signals of PV or SST interneurons associated with sociability in a home cage[35, 36], employing four well-defined social interaction events: nose or genital sniffing, following, and body contact (**Fig. 1D**). The results consistently revealed that social interaction events suppressed the activity of PV or SST interneurons, with a more substantial reduction in calcium signals observed in PV interneurons compared to SST interneurons (**Fig. 1E, F**). Moving forward, we assessed the dynamics of PV and SST interneuron activity during sociability and social preference utilizing a three-chamber test[37]. The patterns of calcium signals for PV and SST interneurons during the initial phase of the test (**Fig. 1G-I**) mirrored those observed during sociability in the home cage (**Fig. 1E, F**). Notably, during the social preference phase, when test mice approached unfamiliar mice (**Fig. 1J**), the changes in calcium signals of SST interneurons were more pronounced than those of PV interneurons (**Fig. 1K, L**).

Furthermore, we conducted a comparative analysis of the dynamic fluctuations in GCaMP levels between PV and SST interneurons at different stages of social interaction behavior (**Fig. 1M-O**). In the sociability within the home cage, the area under the curve (AUC) of the Ca^{2+} signal in PV interneurons surpassed that of SST interneurons (**Fig. 1M left**). While both PV and SST neurons exhibited a significant correlation between AUC and the duration of social events, the correlation slope was notably greater in PV neurons than in SST neurons (**Fig. 1M right**). A similar trend was observed in

sociability within the three-chamber apparatus (**Fig. 1N**). However, during social preference within the three-chamber apparatus, the AUC and correlation slope of SST neurons exceeded those of PV neurons (**Fig. 1O**). These findings collectively suggest that the activity of PV and SST interneurons in the ACC is suppressed during social interaction, with PV interneurons demonstrating heightened sensitivity to sociability and SST interneurons exhibiting more pronounced changes during social preference.

Apoptosis strategy intervention of PV and SST interneurons enhanced the different phases of social interaction

Next, we further investigated whether the inhibition of PV or SST interneurons modulates different phases of social interaction using taCasp3[38]. This approach selectively induced cell-autonomous apoptosis in two types of interneurons, and subsequent examinations unveiled changes in social behavior (**Fig. 2A, B**). We first confirmed that most of the PV and SST interneurons in the ACC were ablated through quantification of the PVALB or SST positive cells and evaluation of the mRNA expression levels of *Pvalb* or *Sst* (**Fig. 2C-E**). PV-Cre mice displayed more intense social interaction in the three-chamber test and showed a heightened preference for unfamiliar companions within their home cage after the taCasp3 virus intervention (**Fig. 2 F-H and K-L**). However, this intervention had negligible effect on socially preferred behavior (**Fig. 2I, J**). Conversely, SST-Cre mice exhibited unaffected sociability (**Fig. 2M, N and R**) but showed a preference for interacting with a stranger object rather than a familiar object in the social preference test (**Fig. 2O-Q**) due to the virus intervention. These findings suggest that PV interneurons exert a more substantial influence on the willingness to socialize, while SST interneurons wield a more potent modulation on social preference.

Activation of PV interneurons led to a more significant decrease in sociability compared to the stimulation of SST interneurons in the home cage

Next, we employed a Cre-dependent expression strategy of Channelrhodopsin-2 (ChR2)

to investigate the impact of exciting PV-positive and SST-positive interneurons on social interaction behavior (**Fig. 3A**). The intent was to elicit firing in these interneurons through a relatively high-frequency light stimulation, aligning with the inherent firing properties of PV and SST interneurons[26, 39]. Our results substantiated that both PV and SST interneurons expressed ChR2 with a probability of over 90% (**Extended Data Fig. 2A, B**). Moreover, we observed that PV interneurons expressing ChR2 exhibited faithful generation of action potentials in response to 40 Hz photo stimulation (**Extended Data Fig. 2C)** inducing c-Fos expression in PV-positive neurons (**Extended Data Fig. 2E**). Similar observations were made for SST interneurons (**Extended Data Fig. 2D, F**). In the home cage, the activation of PV interneurons resulted in a decrease in social exploration behaviors with unfamiliar mice (**Fig. 3B**). Interestingly, social interaction time did not fully recover in PV-ChR2 mice even following the cessation of laser stimulation (**Fig. 3B**). Similarly, the activation of SST interneurons also diminished social events and total social interaction time (**Fig. 3C**), with partial recovery observed upon cessation of photo-stimulation (**Fig. 3C**). An intriguing observation was the gradual decline in social interaction time between test mice and an intruder after contact with the test mice's home cage. To explore the possibility that the effect of ChR2 was influenced by the familiarity of the mice, we compared the correlation of social interaction time differences between the first two stages ($laser_{ON}$-$laser_{OFF}$) and the second two stages ($laser_{OFF}$-$laser_{ON}$). Results revealed that Cre-negative mice exhibited a high correlation slope, suggesting a correlation between the reduction in social interaction and time in this group (**Fig. 3D**). However, both PV and SST neuron excitation led to significantly smaller correlation slope values, indicating a correlation between social interaction impairment and photostimulation in these groups (**Fig. 3D**).

Moreover, when comparing social interaction time during laser treatment among the three groups, the Cre-negative group exhibited the highest social interaction time, while the PV-Cre group demonstrated the shortest time (**Fig. 3E**). Additionally, the inhibition

index of ChR2 stimulation was compared between the PV-Cre and SST-Cre groups, revealing a more pronounced decrease in social events upon the activation of PV interneurons compared to the SST-Cre group (**Fig. 3F**).

Furthermore, when the intruder mouse was replaced with a toy mouse, both the PV-Cre and SST-Cre groups exhibited no difference in social interaction, regardless of the laser on or off status (**Fig. 3G**). Subsequent experiments exploring the effects of optogenetics on social odor recognition in PV-Cre and SST-Cre mice indicated that the activation of PV or SST interneurons did not alter the preference for the urine of a stranger mouse in an open field (**Extended Data Fig. 3**).

Activation of PV or SST interneurons inhibited the different stages of social interaction in the three-chamber test

Then we conducted experiments utilizing a three-chamber test, employing optogenetic activation of PV or SST interneurons. In the initial sociability paradigm, PV-Cre mice exhibited a tendency for interaction with the unfamiliar mouse in the absence of blue light activation (**Fig. 3H, I left**). However, upon activation of PV interneurons by blue light, the mice displayed a preference for the vacant zone (**Fig. 3H, I middle**). Post cessation of laser stimulation, a tendency to return to the social zone was observed, albeit without reaching statistical significance (**Fig. 3H, I right; Extended video 1**). Furthermore, a significant disparity in social discrimination bias emerged between pre-stimulus and during-stimulus periods (**Fig. 3J**). SST interneuron activation also curtailed sociability, albeit with a distinct behavioral pattern from PV-Cre mice. Prior to laser activation, SST-Cre mice exhibited a clear preference for the social zone (**Fig. 3N**, **O left**). However, during laser activation, SST-Cre mice spent comparable durations in the social and empty zones (**Fig. 3N, O middle**), with a return to the social zone upon cessation of SST interneuron excitation (**Fig. 3N, O right; Extended video 2**). Although discrimination scores exhibited a significant difference between laser off and laser on conditions, values for SST-Cre mice approached zero, whereas those for

PV-Cre mice were negative (**Fig. 3J, P**).

In the social preference stage, PV-Cre mice initially favored the stranger zone, a preference attenuated during laser activation (**Fig. 3K, L left and middle**). Upon turning off the laser, mice spent similar durations in both the stranger zone and the original zone (**Fig. 3L right**), with discrimination scores for the second stage showing a significant difference between laser off and laser on conditions (**Fig. 3M**). For SST-Cre mice, photo-stimulation prompted a shift from the stranger zone to the original zone. Although statistical significance was not achieved, the mice still spent more time in the original zone (**Fig. 3Q, R right**), mirroring the negative social discrimination score observed in the first stage, akin to results obtained in PV-Cre mice (**Fig. 3M, S**).

Further comparisons of behavioral changes induced by optogenetic excitation of PV or SST interneurons in the three-chamber test revealed that SST-Cre mice took longer to discontinue engaging in social events during photo-stimulation compared to PV-Cre mice in the first stage (**Fig. 3T**). Despite photo-stimulation reducing latency in both groups compared to the condition without stimulation, the difference in discrimination score between laser on and off conditions was more pronounced in PV-Cre mice than SST-Cre mice (**Fig. 3U**), approaching statistical significance (**Fig. 3U**). In the second stage, PV-Cre mice exhibited a preference for the center zone during blue light activation, while SST-Cre mice showed no discernible preference (**Fig. 3W, X**). The latency to cease the first social event in PV-Cre mice was lengthier than that in SST-Cre mice during photo-stimulation (**Fig. 3V**). Furthermore, the difference in discrimination scores exhibited an inverse pattern compared to the first stage, with SST interneuron excitation producing a larger difference compared to PV interneurons (**Fig. 3Y**). Importantly, these optogenetic stimuli exerted no discernible influence on the motor abilities of the mice (**Extended Data Fig. 4A, B**). In conclusion, the activation of PV or SST interneurons exerts distinct effects on social interaction behavior, with PV interneurons inhibiting sociability and SST interneurons reducing social preference.

Abnormal expression of *Kcnh7* in PV and SST-positive neurons is the cause of heterogeneous social interaction disorder in an autistic mice model

Given that the acute activation of PV or SST interneurons can inhibit distinct stages of the social interaction, our subsequent inquiry aimed to ascertain the presence of risk genes within the ASD model that may induce atypical PV or SST activity, thereby contributing to social impairments. *SHANK3* gene is identified as a high-risk gene for autism, and previous investigations have elucidated social interaction deficits in *Shank3* mutant mice[9, 40-49]. To achieve this objective, ACC tissues were meticulously dissected, and subsequent dissociation was followed by single-cell RNA sequencing (scRNA-seq) utilizing 10X Genomics technology. A total of 17,661 high-quality cells obtained from wild-type (WT) and *Shank3* KO male mice were subjected to comprehensive analysis, with clustering facilitated by Seurat[50]. Employing singleR[51] and manual analysis, seven distinct cell cluster types were identified (**Fig. 4A, B**), with representative marker genes, *Pvalb* and *Sst*, highlighted for simplicity **(Fig. 4C)**. Further scrutiny involved an examination of gene expression differences between neurons exhibiting high *Pvalb* and *Sst* expression, revealing both upregulated and downregulated genes.

Of particular interest among the identified genes was *Kcnh7*, a member of the ether-a-go-go-related gene family, which displayed significant downregulation in both the *Pvalb* and *Sst* clusters (**Fig. 4D left, E left**). *Kcnh7* encodes ERG channels, voltage-gated potassium channels known for inward rectification during repolarization[52]. Notably, accumulating evidence associates *Kcnh7* with ASD, emphasizing its significance in neurobiology[33]. Quantitative analysis of *Kcnh7* expression was carried out through single-cell qRT-PCR with patch-clamp, revealing predominant expression in PV-positive and SST-positive neurons (**Fig. 4D right, E right**). Importantly, *Shank3* KO mice exhibited a significant decrease in *Kcnh7* expression in these neuron populations compared to WT mice, corroborating scRNA-seq findings (**Fig. 4F-G, K-L**). Moreover, PV-positive and SST-positive neurons in *Shank3* mutant mice displayed heightened excitability compared to WT mice (**Fig. 4H, I and M, N**). Administration

of E-4031, an ERG channel blocker, further heightened firing frequency in both PV- and SST-positive neurons (**Extended Data Fig. 5**). Additionally, both neuron types displayed decreased amplitudes of ERG channel currents in *Shank3* KO mice compared to WT mice (**Fig. 4J, O**). Based on these comprehensive findings, we posit that the aberrant expression of the Kv11.3 potassium channel, encoded by *Kcnh7*, in PV- and SST-positive neurons may contribute to heightened excitability, thereby influencing abnormal social interaction behavior observed in *Shank3* KO mice.

To investigate the proposed hypothesis, a Cre-dependent CRISPR–Cas9 viral methodology was employed. A virus expressing target RNAs, in combination with a Cre-dependent SpCas9 virus, was administered to PV-Cre and SST-Cre mice for the purpose of knocking out *Kcnh7* in the ACC (**Fig. 5A**). Immunofluorescent staining analysis validated the predominant presence of the gRNA-GFP virus in PV-positive neurons (**Fig. 5B, C**) and SST-positive neurons (**Fig. 5M, N**). Subsequent quantitative analysis demonstrated a significant reduction in KCNH7 levels within these neurons following the CRISPR–Cas9 viral intervention (**Fig. 5D, O**).

In order to evaluate the impact of *Kcnh7* on neuronal excitability, an examination of action potential components in PV-positive and SST-positive neurons was conducted (**Fig. 5E, F** and **P, Q**). The results indicated alterations in the half-width of the action potential and the first after hyperpolarization component induced by the *Kcnh7*-gRNA virus (**Fig. 5G, R**). Furthermore, PV and SST-positive neurons transduced with the *Kcnh7*-gRNA virus demonstrated a significant increase in the number of action potentials evoked by depolarizing current injections (**Fig. 5H, S**). Subsequent to these neurophysiological investigations, alterations in sociability and social preference were assessed following the CRISPR–Cas9 viral intervention. PV-Cre mice exhibited reduced sociability, spending less time in the social zone and more time in the center zone (**Fig. 5I, J left and right**), so the sociability had prominent differences before and after virus intervention (**Fig. 5K**). Notably, the Cas9 intervention group also displayed diminished sociability, evidenced by similar activity in both the social zone and empty

zone (**Fig. 5L**). In the subsequent phase of the three-chamber test, PV-Cre mice demonstrated decreased time spent in both the stranger social zone and the original social zone (**Extended Data Fig. 6A, B**), with no discernible change in the discrimination score (**Extended Data Fig. 6C**).

The impact of *Kcnh7* knockout on the social preference of SST-Cre mice was then investigated through three-chamber tests. Post-virus injection, SST-Cre mice spent less time in stranger social zone and more time in original zone (**Fig. 5T, U left and middle**). Further analysis revealed a more pronounced decrease in the stranger zone compared to the original zone (**Fig. 5V**). Additionally, SST-Cre mice exhibited abnormal social preference capacity, spending significantly more time in the original social zone (**Fig. 5W**). Initial stages of the three-chamber test also indicated reduced sociability in SST-Cre mice, characterized by decreased time spent in the social zone and increased time in the empty zone (**Extended Data Fig. 6D-F**). These findings suggest distinct roles for PV-positive and SST-positive GABAergic interneurons in social interaction related disorders and emphasize the potential significance of *Kcnh7* in modulating the function of these neurons within the ACC, thereby influencing social behavior.

Specific projections contribute to the differential inhibition on the social interaction behavior of PV and SST interneurons in the ACC

Although the activation of PV or SST neurons can inhibit different phases of social behavior, this regulation is mediated through the influence of pyramidal neurons. Our observations revealed variations in the short-term plasticity of inhibitory synaptic transmission from these interneurons to pyramidal neurons, as well as differences in their firing patterns (**Extended Data Fig. 7**). Additionally, the distinct impact of these interneurons may be linked to the differences in the projections received by each type of interneuron. Subsequently, we embarked on an investigation aimed at elucidating a potential circuit mechanism underlying the observed discrepancy in social interaction ability between PV and SST interneurons. Our approach involved employing whole-

brain retrograde tracing using rabies viral vectors (RVs) that were modified with engineered rabies glycoprotein (RG) deletion[53]. PV-Cre or SST-Cre mice were injected with an adeno-associated virus (AAV) helper vector and AAV-double-floxed inverted open reading frame (DIO)-RVG, enabling the visualization of starter neurons and providing essential components for retrograde tracing. Subsequently, RV-EnvA-ΔG-dsRed was injected after a three-week interval to label neurons expressing the required components (**Fig. 6A**).

The results exhibited that the starter neurons were predominantly situated in the ACC, with a lesser presence in the adjacent PFC region (**Fig. 6B, C and E**). Subsequent analysis of the number of cells per unit area upstream was conducted by referencing The Mouse Brain in Stereotaxic Coordinates (second edition), revealing that both PV and SST interneurons shared comparable upstream afferents. Particularly, the lateral posterior thalamic nucleus (LPMR) exhibited heightened expression upstream of PV-positive neurons, while the ventral hippocampus (vHPC) displayed elevated expression upstream of SST neurons (**Fig. 6D, F**).

To delve into the synaptic connectivity type between LPMR and PV interneurons in the ACC, optogenetics and whole-cell patch-clamping techniques were employed in brain slices. The results exhibited that LPMR formed an excitatory monosynaptic projection to PV interneurons (**Extended Data Fig. 8A, B**). Similarly, the projection from the ventral hippocampus (vHPC) to SST interneurons in the ACC demonstrated the same type of connectivity (**Extended Data Fig. 8A, C**). To further corroborate these projections *in vivo*, GCaMP7 expression on PV or SST interneurons in the ACC was achieved using a Cre-dependent strategy, and ChR2 was expressed upstream of the ACC using the AAV2-retro serotype (**Extended Data Fig. 8D, G**). An optic fiber was implanted into the LPMR or vHPC for upstream excitation, while another fiber was inserted into the ACC to record the GCaMP7 signaling of PV or SST interneurons receiving the projection from upstream. Activation of LPMR or vHPC through 40 Hz 473 nm photo stimulation significantly elevated the calcium signaling of PV or SST

interneurons in the ACC (**Extended Data Fig. 8F, I**), thereby affirming the existence of these two pathways from both morphological and functional perspectives.

Subsequently, we sought to elucidate whether the delineated pathways were implicated in the distinct modulation of social behavior by PV and SST interneurons within the ACC. AAV1-Flp-EGFP[54] was injected into the LPMR of PV-Cre mice to achieve transmonosynaptic anterograde expression of Flp in the postsynaptic neurons of LPMR, including those within the ACC. Concurrently, AAV-hSyn-Con-Fon-ChR2-mCherry[55] was injected into the ACC to facilitate the expression of ChR2 in PV interneurons innervated by LPMR (**Fig. 7A-C**).

Subsequent social interaction tests in the home cage and three-chamber were conducted, during which photoactivation was temporally coordinated as in previous experiments (**Fig. 3**). The outcomes revealed that the activation of PV interneurons in the LPMR-ACC pathway led to a reduction in social interaction time in the home cage (**Fig. 7D, E**) and an augmented preference for the empty zone in the three-chamber setup (**Fig. 7H-J**). And mCherry-control group had no significant effect on social behavior in home cage test (**Fig. 7F, G**). Importantly, in the second phase of the three-chamber test, this pathway did not significantly alter normal social appetitive behavior (**Extended Data Fig. 9A, B**). Additionally, we identified projections from the ventral hippocampus (vHPC) to PV-positive interneurons in the ACC. However, selectively exciting the vHPC to PV-positive interneurons projection did not markedly influence preference behavior in the second part of the three-chamber test (**Fig. 7K**).

Employing a similar strategy, we activated the projection from the vHPC to SST-positive interneurons in the ACC and assessed its impact on social preference behavior (**Fig. 7L-N**). Results indicated that the specific regulation of the vHPC to SST interneurons influenced social preference behavior (**Fig. 7O-Q**) in SST-Cre mice during the three-chamber test. In the mCherry-control group, the excitation of SST interneurons in this projection did not result in significant changes in social preference

compared to the ChR2 group (**Fig. 7R, S**). Furthermore, the stimulation did not significantly alter the active social exploration behavior of the SST-Cre mice in the first phase of the three-chamber test (**Extended Data Fig. 9C**, **D**). Collectively, these findings affirm our hypothesis that the targeted regulation of these two circuits can potentially serve as a strategy to address the heterogeneity of social interaction disorders.

Discussion

Projection neurons are functional executors across diverse brain regions, leveraging their axons to convey essential instructions to downstream targets. However, the precision of projection neuron performance is not solely reliant on intrinsic factors. It is significantly influenced by local interneurons, contributing to diverse regulatory mechanisms, including feedback and feedforward processes[56, 57]. Previous extensive research have delved into their functions in crucial cognitive domains such as working memory[58], flexibility[59], and various other facets[34, 60-62]. This underscores the essential need to comprehend the specific contributions of interneurons within a given brain region. In this study, our attention focused on two primary interneuron subtypes within the ACC: PV and SST interneurons. We found that PV and SST interneurons in the ACC exert distinct effects on social interaction behavior. Specifically, PV interneurons exhibit heightened sensitivity to sociability, while SST interneurons show more pronounced changes during social preference. In a *Shank3* autistic model, the *Kcnh7* gene, a known risk gene for ASD, was found to be reduced in the PV and SST interneurons of the ACC. Deletion of *Kcnh7* specifically in PV or SST interneurons in the ACC contributes to the variability of social interaction disorders. Additionally, the specific pathways from LPMR to PV and vHPC to SST in the ACC represent a potential mechanism for generating the differential roles of these interneurons. Our findings suggest that both types of interneurons in the ACC are involved in the regulation of social interaction, exhibiting differentiation in their regulatory functions. PV interneurons are implicated in regulating social abilities, while SST interneurons are

more involved in regulating social preferences. This finding aligns with observations of PV and SST interneurons in other behavioral paradigms, confirming the distinct roles of different interneuron types in regulating projection neurons[58-61].

Given the distinct regulatory roles of PV and SST interneurons in modulating projection neurons and their potential implications for the functioning of the relevant brain area, it is imperative to delve into the underlying mechanisms. This exploration is not only crucial for understanding social behavior but also holds the promise of providing insights into associated disorders, such as ASD. Recent studies have demonstrated that these two neuron types may exhibit varying sensitivities to the same stimuli in hippocampus[63] and cortex[64]. Notably, the KO of *Mecp2*, a high-risk gene for autism, in either PV or SST neurons in the hypothalamus yields significantly different phenotypes in mice, mirroring the distinct manifestations of Rett syndrome[65]. Intriguingly, our present work found that selectively knocking out *Kcnh7*, a susceptibility gene for ASD [33, 66], in PV or SST neurons can impair social ability or social preference, respectively. The downregulation of *Kcnh7* gene expression was found in PV and SST neurons in *Shank3* KO mice, a model of autism primarily associated with excitatory synaptic dysfunction in projection neurons. As KCNH7 serves as an inward rectifying potassium channel crucial for regulating neuronal excitability[52, 67], the downregulation of its expression could result in heightened excitability in PV and SST neurons (**Fig. 5**). This augmented excitability in PV and SST neurons has been associated with impaired social interaction, as corroborated by our optogenetic experiments (**Fig. 3**). These collective findings strongly indicate that the phenotypic abnormalities observed in *Shank3* KO mice are not solely ascribed to projection neuron abnormalities but likely involve interneurons. Indeed, our observations reveal that sensory hypersensitivity in this model is associated with interneuron abnormalities[68]. These results underscore that PV and SST neurons, despite exposure to the same stimuli, elicit distinct responses. The differential regulation of projection neurons by these interneurons may thus contribute to variations in social behavior. Moreover, this insight into the intricate interplay

between molecular (such as *Shank3* and *Kcnh7*), cellular (PV neurons, SST neurons, and projection neurons), and behavioral phenomena enhances our understanding of the neurobiological underpinnings of social dysfunction and related disorders.

While the involvement of PV or SST interneurons is integral to the regulation of social interaction, the synaptic inputs into these interneurons play a pivotal role in their operations. Notably, glutamatergic axons originating from projection neurons in the mediodorsal thalamic nucleus selectively target PV neurons in ACC, initiating feedforward inhibition of pyramidal neurons in layer 3 of the ACC and thereby impacting cognitive flexibility[27]. Additionally, axons emanating from hippocampal neurons that target SST neurons in the medial prefrontal cortex (mPFC) have been shown to influence the accuracy of working memory[69]. These insights underscore the significance of projections from diverse brain regions to PV and SST neurons as potential mechanisms governing the distinctive roles of these interneuron types. Our research further reveals that, despite receiving similar inputs, PV and SST neurons exhibit differentiation in input, potentially contributing to the distinct regulation of social interaction functions. Specifically, our observations indicate that LPMR projecting to PV neurons in the ACC are involved in regulating social ability, whereas vHPC projecting to SST neurons in the ACC play a key role in regulating social preference. The LPMR, a crucial region implicated in the attention network[70], establishes connections with the visual cortex, parietal cortex, and ACC[71-73]. Anomalies in connectivity between the LPMR and cortex, coupled with a thinner parietal cortex and atypical visual processing observed in individuals with ASD[74-76], suggest that attention networks involving the LPMR play a crucial role in processing social relation information and related disorders such as ASD. Concerning the HPC, it has been traditionally implicated in social preference[77, 78]. However, recent research proposes that the vHPC modulates social memory through PV neurons in the mPFC[79]. Intriguingly, a substantial body of evidence highlights contrasting roles of the ACC and mPFC in social behavior in mice[22, 23, 80]. This observation implies that the ACC and

mPFC may possess distinct functional characteristics contributing to social behavior in murine models. This nuanced understanding of the interconnected brain regions and their differential roles enhances our grasp of the neurobiological underpinnings of social behavior, providing valuable insights into potential therapeutic avenues for disorders associated with social dysfunction.

Moreover, it is imperative to acknowledge the involvement of brain regions beyond the ACC in the intricate modulation of social behavior. Recent investigations highlight the participation of SST neurons in the mPFC in mediating disinhibition, functioning as a pivotal circuit mechanism to regulate social fear behavior[23]. Additionally, Zhang et al. reported the formation of a disinhibitory microcircuit in the dorsomedial prefrontal cortex involving VIP, PV, and pyramidal neurons, governing social competition in mice [24]. Numerous comprehensive reviews have delved into the neural circuitry underpinning social behavior[1, 81-83]. Furthermore, the cortex houses a myriad of interneuron types beyond the aforementioned PV and SST interneurons. Our recent discovery underscores the role of cholecystokinin interneurons in the ACC, revealing their contribution to social isolation-induced social impairments. This finding suggests a broader involvement of various interneuron types in social interaction[84]. A comprehensive investigation utilizing electrophysiological, morphological, and transcriptomic analyses has identified 28 distinct classifications of interneurons within the visual cortex of mice[85]. However, fully understanding the roles played by these diverse subtypes of interneurons remains a challenging endeavor. Further research is imperative to develop reliable analytical techniques capable of elucidating the intricate relationship between interneuron subtypes characterized by molecular markers and those characterized by their functional activities. This pursuit is essential for unraveling the complex network of interactions that govern social behavior at the neural level.

To the best of our knowledge, the present research provides strong evidence that PV and SST interneurons in the ACC play a distinct role in social interaction. Specifically, our findings highlight that PV-positive interneurons predominantly regulate sociability,

while SST-positive interneurons play a more significant role in shaping social preference behaviors. The nuanced roles exhibited by these interneuron types during social interaction within the ACC likely contribute to the diverse manifestations of social interaction deficits. This insight opens new avenues for understanding and potentially addressing related disorders, particularly autism, shedding light on novel therapeutic approaches grounded in the specific functions of PV and SST interneurons in the intricate network governing social behaviors.

Acknowledgements

We thank Prof. Guoping Feng (Massachusetts Institute of Technology) for suggestions and discussions. This study was supported by the Science and Technology Innovation 2030 Project of China (2021ZD0201005 to S. W.), the Natural Science Foundation of China (32394032, 82221001 to S.W., 82271577, 82071536 to W.W., 82271578 to Q.C.), the Shaanxi Provincial Key Research and Development Program (2020ZDLSF01–09 to S. W.), the Shaanxi Provincial Innovation Chain Project of Key Industries (2023-ZDLSF-47 to W.W.), Shanghai Pujiang program (22PJ1415500 to Q.C.) and Zhongshan Municipal Bureau of Science and Technology grant (CXTD2022013 to Q.C.) Guangdong province High-level Innovative Research Institute project (2021B0909050003, Q.C.)

Author Contributions C. Q., Q. C., W. W., and S. W. designed the experiments. C. Q., W. S., H. M., E. H., J. G., M. D., A. C., and Q. X. performed the experiments and analysed the data. C. Q., W. S., H. M., Q. C., W. W., and S. W. interpreted the data. C. Q., Q. C., W. W., and S. W. wrote the paper.

Competing Financial Interests statement

The authors declare no competing financial interests.

Author Information Reprints and permissions information are available at

www.nature.com/reprints. The authors declare no competing financial interests. Readers are welcome to comment on the online version of the paper. Correspondence and requests for materials should be addressed to S.W. (shengxi@fmmu.edu.cn) or W. W. (wwt0657@fmmu.edu.cn) or Q. C. (chenqian@zidd.ac.cn).

Reference

1. Chen, P. & Hong, W. Neural Circuit Mechanisms of Social Behavior. *Neuron* **98**, 16-30 (2018).
2. Park, G., *et al.* Social isolation impairs the prefrontal-nucleus accumbens circuit subserving social recognition in mice. *Cell Rep* **35**, 109104 (2021).
3. Almeida-Santos, A.F., *et al.* Social isolation impairs the persistence of social recognition memory by disturbing the glutamatergic tonus and the olfactory bulb-dorsal hippocampus coupling. *Sci. Rep.* **9**, 473 (2019).
4. Kanwisher, N. & Yovel, G. The fusiform face area: a cortical region specialized for the perception of faces. *Philos. Trans. R. Soc. Lond. B Biol. Sci.* **361**, 2109-2128 (2006).
5. Moy, S.S., *et al.* Sociability and preference for social novelty in five inbred strains: an approach to assess autistic-like behavior in mice. *Genes Brain Behav* **3**, 287-302 (2004).
6. Bicks, L.K., Koike, H., Akbarian, S. & Morishita, H. Prefrontal Cortex and Social Cognition in Mouse and Man. *Front. Psychol.* **6**, 1805 (2015).
7. Walsh, J.J., Christoffel, D.J. & Malenka, R.C. Neural circuits regulating prosocial behaviors. *Neuropsychopharmacology* **48**, 79-89 (2023).
8. van den Berg, P. & Wenseleers, T. Uncertainty about social interactions leads to the evolution of social heuristics. *Nat Commun* **9**, 2151 (2018).
9. Peça, J., *et al.* Shank3 mutant mice display autistic-like behaviours and striatal dysfunction. *Nature* **472**, 437-442 (2011).
10. Chevallier, C., Kohls, G., Troiani, V., Brodkin, E.S. & Schultz, R.T. The social motivation theory of autism. *Trends Cogn. Sci.* **16**, 231-239 (2012).
11. Apps, M.A., Rushworth, M.F. & Chang, S.W. The Anterior Cingulate Gyrus and Social Cognition: Tracking the Motivation of Others. *Neuron* **90**, 692-707 (2016).
12. Lockwood, P.L. The anatomy of empathy: Vicarious experience and disorders of social cognition. *Behav. Brain Res.* **311**, 255-266 (2016).
13. Etkin, A., Egner, T. & Kalisch, R. Emotional processing in anterior cingulate and medial prefrontal cortex. *Trends Cogn. Sci.* **15**, 85-93 (2011).
14. Seamans, J.K. & Floresco, S.B. Event-based control of autonomic and emotional states by the anterior cingulate cortex. *Neurosci. Biobehav. Rev.* **133**, 104503 (2022).
15. Walton, M.E., Croxson, P.L., Behrens, T.E., Kennerley, S.W. & Rushworth, M.F. Adaptive decision making and value in the anterior cingulate cortex. *Neuroimage* **36 Suppl 2**, T142-154 (2007).
16. López-Solà, M., Geuter, S., Koban, L., Coan, J.A. & Wager, T.D. Brain mechanisms of social touch-induced analgesia in females. *Pain* **160**, 2072-2085 (2019).
17. Rudebeck, P.H., Buckley, M.J., Walton, M.E. & Rushworth, M.F. A role for the macaque anterior cingulate gyrus in social valuation. *Science* **313**, 1310-1312 (2006).
18. Wittmann, M.K., Lockwood, P.L. & Rushworth, M.F.S. Neural Mechanisms of Social Cognition in Primates. *Annu. Rev. Neurosci.* **41**, 99-118 (2018).
19. Assaf, M., *et al.* Abnormal functional connectivity of default mode sub-networks in autism spectrum disorder patients. *Neuroimage* **53**, 247-256 (2010).
20. Laidi, C., *et al.* Decreased Cortical Thickness in the Anterior Cingulate Cortex in Adults with Autism. *J. Autism Dev. Disord.* **49**, 1402-1409 (2019).
21. Hou, Y., *et al.* LF-rTMS ameliorates social dysfunction of FMR1(-/-) mice via modulating Akt/GSK-3β signaling. *Biochem. Biophys. Res. Commun.* **550**, 22-29 (2021).
22. Guo, B., *et al.* Anterior cingulate cortex dysfunction underlies social deficits in Shank3 mutant mice. *Nat Neurosci* **22**, 1223-1234 (2019).
23. Xu, H., *et al.* A Disinhibitory Microcircuit Mediates Conditioned Social Fear in the Prefrontal

Cortex. *Neuron* **102**, 668-682.e665 (2019).
24. Zhang, C.*, et al.* Dynamics of a disinhibitory prefrontal microcircuit in controlling social competition. *Neuron* **110**, 516-531.e516 (2022).
25. Jiang, C.*, et al.* Morphine coordinates SST and PV interneurons in the prelimbic cortex to disinhibit pyramidal neurons and enhance reward. *Mol. Psychiatry* **26**, 1178-1193 (2021).
26. Tremblay, R., Lee, S. & Rudy, B. GABAergic Interneurons in the Neocortex: From Cellular Properties to Circuits. *Neuron* **91**, 260-292 (2016).
27. Delevich, K., Tucciarone, J., Huang, Z.J. & Li, B. The mediodorsal thalamus drives feedforward inhibition in the anterior cingulate cortex via parvalbumin interneurons. *J. Neurosci.* **35**, 5743-5753 (2015).
28. Prasad, J.A., Carroll, B.J. & Sherman, S.M. Layer 5 Corticofugal Projections from Diverse Cortical Areas: Variations on a Pattern of Thalamic and Extrathalamic Targets. *J. Neurosci.* **40**, 5785-5796 (2020).
29. Sun, Q.*, et al.* A whole-brain map of long-range inputs to GABAergic interneurons in the mouse medial prefrontal cortex. *Nat. Neurosci.* **22**, 1357-1370 (2019).
30. Ferguson, B.R. & Gao, W.J. Thalamic Control of Cognition and Social Behavior Via Regulation of Gamma-Aminobutyric Acidergic Signaling and Excitation/Inhibition Balance in the Medial Prefrontal Cortex. *Biol. Psychiatry* **83**, 657-669 (2018).
31. Bhat, S., Acharya, U.R., Adeli, H., Bairy, G.M. & Adeli, A. Autism: cause factors, early diagnosis and therapies. *Rev. Neurosci.* **25**, 841-850 (2014).
32. Lai, M.C., Lombardo, M.V. & Baron-Cohen, S. Autism. *Lancet* **383**, 896-910 (2014).
33. Griswold, A.J.*, et al.* Targeted massively parallel sequencing of autism spectrum disorder-associated genes in a case control cohort reveals rare loss-of-function risk variants. *Mol. Autism* **6**, 43 (2015).
34. Kvitsiani, D.*, et al.* Distinct behavioural and network correlates of two interneuron types in prefrontal cortex. *Nature* **498**, 363-366 (2013).
35. Felix-Ortiz, A.C. & Tye, K.M. Amygdala inputs to the ventral hippocampus bidirectionally modulate social behavior. *J. Neurosci.* **34**, 586-595 (2014).
36. Nasu, M.*, et al.* Reduced home cage and social activity in Pou3f2⊿ mice. *Biochem. Biophys. Res. Commun.* **523**, 411-415 (2020).
37. O'Tuathaigh, C.M.*, et al.* Phenotypic characterization of spatial cognition and social behavior in mice with 'knockout' of the schizophrenia risk gene neuregulin 1. *Neuroscience* **147**, 18-27 (2007).
38. Gray, D.C., Mahrus, S. & Wells, J.A. Activation of specific apoptotic caspases with an engineered small-molecule-activated protease. *Cell* **142**, 637-646 (2010).
39. Hu, H., Gan, J. & Jonas, P. Interneurons. Fast-spiking, parvalbumin^{+} GABAergic interneurons: from cellular design to microcircuit function. *Science* **345**, 1255263 (2014).
40. Monteiro, P. & Feng, G. SHANK proteins: roles at the synapse and in autism spectrum disorder. *Nat. Rev. Neurosci.* **18**, 147-157 (2017).
41. Bozdagi, O.*, et al.* Haploinsufficiency of the autism-associated Shank3 gene leads to deficits in synaptic function, social interaction, and social communication. *Mol. Autism* **1**, 15 (2010).
42. Wang, X.*, et al.* Synaptic dysfunction and abnormal behaviors in mice lacking major isoforms of Shank3. *Hum. Mol. Genet.* **20**, 3093-3108 (2011).
43. Kouser, M.*, et al.* Loss of predominant Shank3 isoforms results in hippocampus-dependent impairments in behavior and synaptic transmission. *J. Neurosci.* **33**, 18448-18468 (2013).
44. Lee, J.*, et al.* Shank3-mutant mice lacking exon 9 show altered excitation/inhibition balance, enhanced rearing, and spatial memory deficit. *Front. Cell. Neurosci.* **9**, 94 (2015).
45. Speed, H.E.*, et al.* Autism-Associated Insertion Mutation (InsG) of Shank3 Exon 21 Causes Impaired Synaptic Transmission and Behavioral Deficits. *J. Neurosci.* **35**, 9648-9665 (2015).
46. Jaramillo, T.C.*, et al.* Altered Striatal Synaptic Function and Abnormal Behaviour in Shank3 Exon4-9 Deletion Mouse Model of Autism. *Autism Res.* **9**, 350-375 (2016).
47. Mei, Y.*, et al.* Adult restoration of Shank3 expression rescues selective autistic-like phenotypes. *Nature* **530**, 481-484 (2016).
48. Wang, X.*, et al.* Altered mGluR5-Homer scaffolds and corticostriatal connectivity in a Shank3 complete knockout model of autism. *Nat Commun* **7**, 11459 (2016).
49. Zhou, Y.*, et al.* Mice with Shank3 Mutations Associated with ASD and Schizophrenia Display Both Shared and Distinct Defects. *Neuron* **89**, 147-162 (2016).

50. Butler, A., Hoffman, P., Smibert, P., Papalexi, E. & Satija, R. Integrating single-cell transcriptomic data across different conditions, technologies, and species. *Nat. Biotechnol.* **36**, 411-420 (2018).
51. Aran, D.*, et al.* Reference-based analysis of lung single-cell sequencing reveals a transitional profibrotic macrophage. *Nat. Immunol.* **20**, 163-172 (2019).
52. Xiao, K.*, et al.* ERG3 potassium channel-mediated suppression of neuronal intrinsic excitability and prevention of seizure generation in mice. *J. Physiol.* **596**, 4729-4752 (2018).
53. Callaway, E.M. & Luo, L. Monosynaptic Circuit Tracing with Glycoprotein-Deleted Rabies Viruses. *J. Neurosci.* **35**, 8979-8985 (2015).
54. Zingg, B., Peng, B., Huang, J., Tao, H.W. & Zhang, L.I. Synaptic Specificity and Application of Anterograde Transsynaptic AAV for Probing Neural Circuitry. *J Neurosci* **40**, 3250-3267 (2020).
55. Poulin, J.F.*, et al.* Mapping projections of molecularly defined dopamine neuron subtypes using intersectional genetic approaches. *Nat Neurosci* **21**, 1260-1271 (2018).
56. Luo, L. Architectures of neuronal circuits. *Science* **373**, eabg7285 (2021).
57. Kepecs, A. & Fishell, G. Interneuron cell types are fit to function. *Nature* **505**, 318-326 (2014).
58. Kim, D.*, et al.* Distinct Roles of Parvalbumin- and Somatostatin-Expressing Interneurons in Working Memory. *Neuron* **92**, 902-915 (2016).
59. Jeong, H., Kim, D., Song, M., Paik, S.B. & Jung, M.W. Distinct roles of parvalbumin- and somatostatin-expressing neurons in flexible representation of task variables in the prefrontal cortex. *Prog. Neurobiol.* **187**, 101773 (2020).
60. Chen, G.*, et al.* Distinct Inhibitory Circuits Orchestrate Cortical beta and gamma Band Oscillations. *Neuron* **96**, 1403-1418.e1406 (2017).
61. Natan, R.G., Rao, W. & Geffen, M.N. Cortical Interneurons Differentially Shape Frequency Tuning following Adaptation. *Cell Rep* **21**, 878-890 (2017).
62. Pinto, L. & Dan, Y. Cell-Type-Specific Activity in Prefrontal Cortex during Goal-Directed Behavior. *Neuron* **87**, 437-450 (2015).
63. Sharma, V.*, et al.* eIF2α controls memory consolidation via excitatory and somatostatin neurons. *Nature* **586**, 412-416 (2020).
64. Bernard, C.*, et al.* Cortical wiring by synapse type-specific control of local protein synthesis. *Science* **378**, eabm7466 (2022).
65. Ito-Ishida, A., Ure, K., Chen, H., Swann, J.W. & Zoghbi, H.Y. Loss of MeCP2 in Parvalbumin-and Somatostatin-Expressing Neurons in Mice Leads to Distinct Rett Syndrome-like Phenotypes. *Neuron* **88**, 651-658 (2015).
66. Belengeanu, V.*, et al.* A de novo 2.3 Mb deletion in 2q24.2q24.3 in a 20-month-old developmentally delayed girl. *Gene* **539**, 168-172 (2014).
67. Yildirim, C. & Bal, R. ERG Channels Regulate Excitability in Stellate and Bushy Cells of Mice Ventral Cochlear Nucleus. *J. Membr. Biol.* **251**, 711-722 (2018).
68. Chen, Q.*, et al.* Dysfunction of cortical GABAergic neurons leads to sensory hyper-reactivity in a Shank3 mouse model of ASD. *Nat. Neurosci.* **23**, 520-532 (2020).
69. Abbas, A.I.*, et al.* Somatostatin Interneurons Facilitate Hippocampal-Prefrontal Synchrony and Prefrontal Spatial Encoding. *Neuron* **100**, 926-939.e923 (2018).
70. Fiebelkorn, I.C. & Kastner, S. Functional Specialization in the Attention Network. *Annu. Rev. Psychol.* **71**, 221-249 (2020).
71. Kirchgessner, M.A., Franklin, A.D. & Callaway, E.M. Distinct "driving" versus "modulatory" influences of different visual corticothalamic pathways. *Curr. Biol.* **31**, 5121-5137.e5127 (2021).
72. Leow, Y.N.*, et al.* Brain-wide mapping of inputs to the mouse lateral posterior (LP/Pulvinar) thalamus-anterior cingulate cortex network. *J. Comp. Neurol.* **530**, 1992-2013 (2022).
73. Allen, A.E., Procyk, C.A., Howarth, M., Walmsley, L. & Brown, T.M. Visual input to the mouse lateral posterior and posterior thalamic nuclei: photoreceptive origins and retinotopic order. *J. Physiol.* **594**, 1911-1929 (2016).
74. Green, S.A., Hernandez, L., Bookheimer, S.Y. & Dapretto, M. Reduced modulation of thalamocortical connectivity during exposure to sensory stimuli in ASD. *Autism Res.* **10**, 801-809 (2017).
75. Wallace, G.L., Dankner, N., Kenworthy, L., Giedd, J.N. & Martin, A. Age-related temporal and parietal cortical thinning in autism spectrum disorders. *Brain* **133**, 3745-3754 (2010).

76. Robertson, C.E. & Baron-Cohen, S. Sensory perception in autism. *Nat. Rev. Neurosci.* **18**, 671-684 (2017).
77. Montagrin, A., Saiote, C. & Schiller, D. The social hippocampus. *Hippocampus* **28**, 672-679 (2018).
78. Okuyama, T., Kitamura, T., Roy, D.S., Itohara, S. & Tonegawa, S. Ventral CA1 neurons store social memory. *Science* **353**, 1536-1541 (2016).
79. Sun, Q.*, et al.* Ventral Hippocampal-Prefrontal Interaction Affects Social Behavior via Parvalbumin Positive Neurons in the Medial Prefrontal Cortex. *iScience* **23**, 100894 (2020).
80. Yizhar, O.*, et al.* Neocortical excitation/inhibition balance in information processing and social dysfunction. *Nature* **477**, 171-178 (2011).
81. Sato, M., Nakai, N., Fujima, S., Choe, K.Y. & Takumi, T. Social circuits and their dysfunction in autism spectrum disorder. *Mol. Psychiatry* **28**, 3194-3206 (2023).
82. Modi, M.E. & Sahin, M. A unified circuit for social behavior. *Neurobiol. Learn. Mem.* **165**, 106920 (2019).
83. Brecht, M. & Hu, H. Editorial overview: The social brain. *Curr. Opin. Neurobiol.* **68**, iii-v (2021).
84. Guo, B.*, et al.* CB1R dysfunction of inhibitory synapses in the ACC drives chronic social isolation stress-induced social impairments in male mice. *Neuron* (2023).
85. Gouwens, N.W.*, et al.* Integrated Morphoelectric and Transcriptomic Classification of Cortical GABAergic Cells. *Cell* **183**, 935-953.e919 (2020).
86. Ährlund-Richter, S.*, et al.* A whole-brain atlas of monosynaptic input targeting four different cell types in the medial prefrontal cortex of the mouse. *Nat. Neurosci.* **22**, 657-668 (2019).
87. Chen, A.X.*, et al.* Specific Hypothalamic Neurons Required for Sensing Conspecific Male Cues Relevant to Inter-male Aggression. *Neuron* **108**, 763-774.e766 (2020).
88. Qi, C.*, et al.* Excitatory and Inhibitory Synaptic Imbalance Caused by Brain-Derived Neurotrophic Factor Deficits During Development in a Valproic Acid Mouse Model of Autism. *Front. Mol. Neurosci.* **15**, 860275 (2022).
89. Matsuoka, T.*, et al.* Kv11 (ether-à-go-go-related gene) voltage-dependent K(+) channels promote resonance and oscillation of subthreshold membrane potentials. *J. Physiol.* **599**, 547-569 (2021).
90. Del-Aguila, J.L.*, et al.* A single-nuclei RNA sequencing study of Mendelian and sporadic AD in the human brain. *Alzheimers Res. Ther.* **11**, 71 (2019).
91. Camp, J.G.*, et al.* Multilineage communication regulates human liver bud development from pluripotency. *Nature* **546**, 533-538 (2017).

Figures and Figure legends

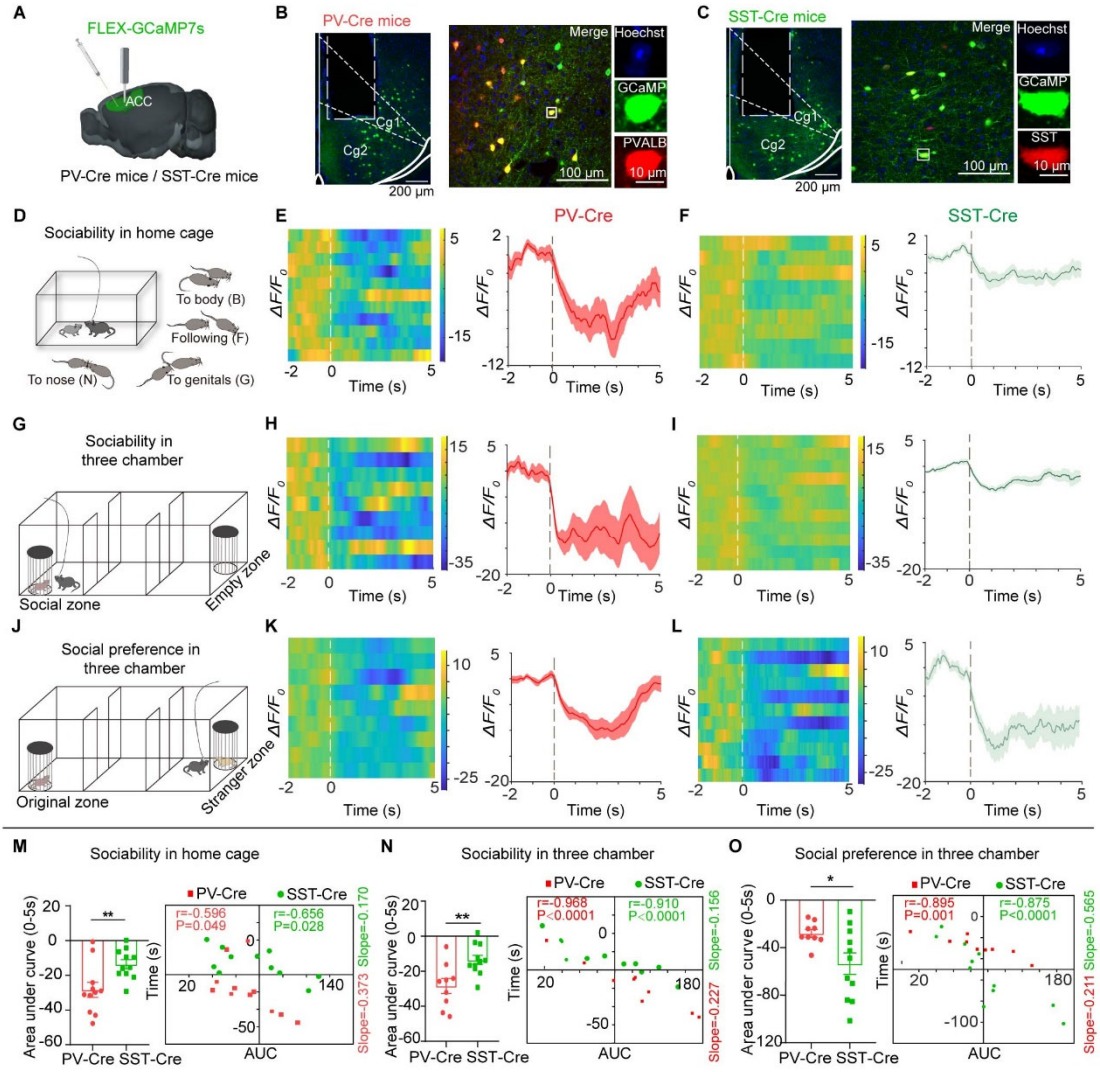

Fig. 1 PV and SST interneurons show varied activities dynamics during social interaction behavior. A. Schematic of FLEX-GCaMP7s injection into the ACC of PV-Cre mice and SST-Cre mice. **B.** Representative image showing the placement of an optic fiber for fiber photometry in the ACC of a PV-Cre mouse injected with GCaMP7s (left) and GCaMP7s expression in the ACC (right). **C.** Representative micrograph showing the placement of an optic fiber for fiber photometry in the ACC of an SST-Cre mouse injected with GCaMP7s (left) and GCaMP7s expression in the ACC (right). **D.** Schematic of social recognition behavior in the home cage. **E.** Ca^{2+} signals associated with social recognition in the home cage. Left panel, the heatmap illustration of Ca^{2+} signals aligned to the onset of each social recognition behavior (to nose, to body,

following or to genitals). Each row represents one mouse. The color scale on the right indicates $\triangle F/F_0$. Right panel, the peri-event plot of the average Ca^{2+} transients. Thick lines indicate the mean, and shaded areas indicate the SEM. Dotted line indicates the moment of contact with the social object. **F.** The same as **E** but for SST-Cre mice. **G.** Schematic of active social behavior in the three-chamber test. **H-I.** The same as **E** but for PV-Cre mice (**H**) and SST-Cre mice (**I**) in three-chamber test for active social behavior. Dotted line indicates the moment of contact with the cage of the social object. **J.** Schematic of social preference behavior in the three-chamber test. **K-L.** The same as **E** and **F** but for PV-Cre mice (**K**) and SST-Cre mice (**L**) in three-chamber for social preference behavior. Dotted line indicates the moment of contact with the cage of the stranger social object. **M.** Area under curve in home cage test (left) and the correlation index between social duration and neuronal activities in PV-Cre and SST-Cre groups (right). **N.** Area under curve in first phase of three-chamber test (left) and the correlation index between social duration and neuronal activities in PV-Cre and SST-Cre groups (right). **O.** Area under curve in second phase of three-chamber test (left) and the slope function compares the change in PV-Cre and SST-Cre groups (right). Data are presented as the mean ± s.e.m. *p<0.05, **p<0.01.

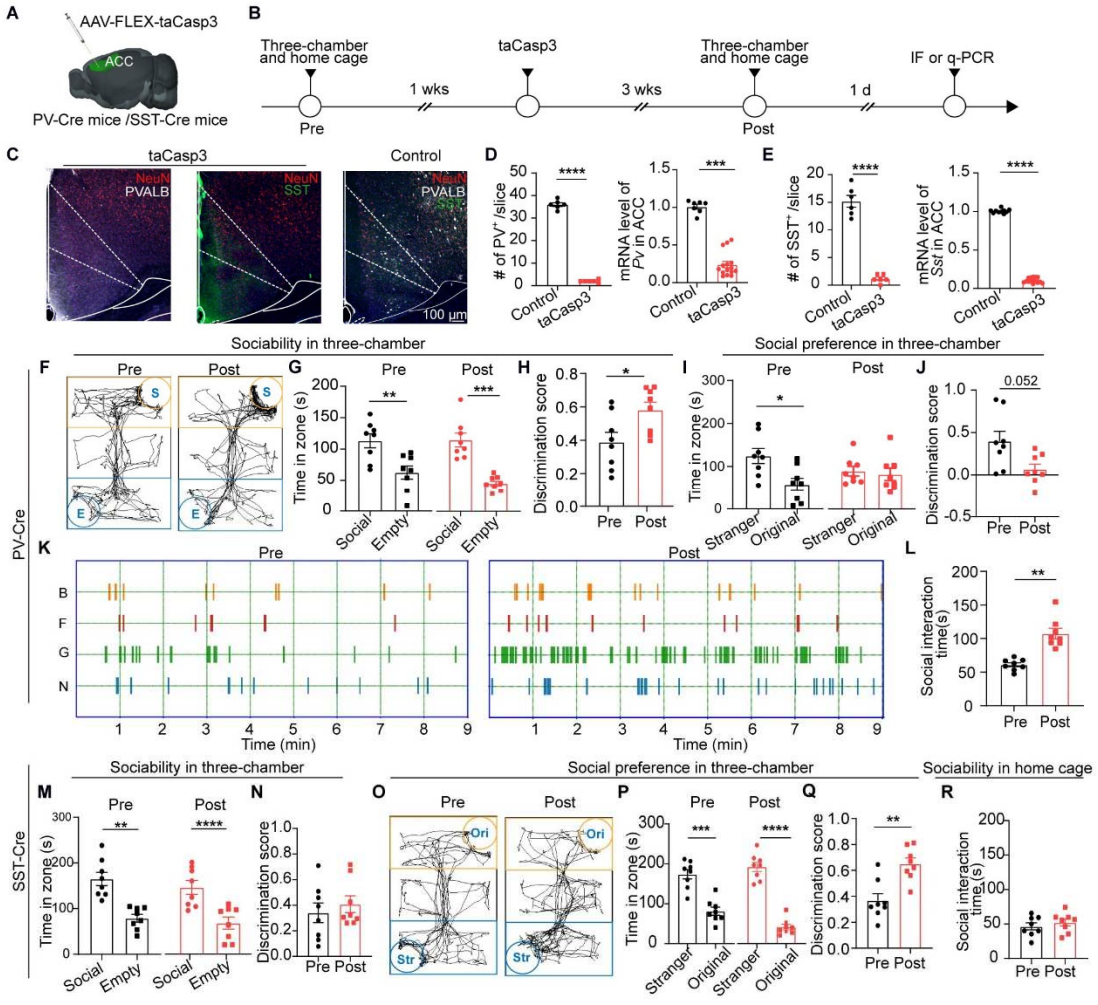

753

754 **Fig. 2 The apoptosis strategy intervention of PV and SST interneurons improved**
755 **various stages of social interaction. A.** Schematic of FLEX-taCasp3 injection into the
756 ACC of PV-Cre mice and SST-Cre mice. **B.** Timeline of this test. **C.** The results of IF
757 between the intervention group and the control group. **D.** Quantification of PV^+ cells
758 between the intervention group and the control group (left) and quantification of mRNA
759 levels of *Pvalb* between the intervention group and the control group (right). **E.** The
760 same of **C** and **D** but of SST-Cre mice. **F.** Traces of PV-Cre mice before (left) and after
761 (right) virus intervention in the sociability test. **G-H.** Quantification of time spent (**G**)
762 and discrimination score (**H**) showing that PV-Cre mice spent more time in the social
763 zone after intervention (discrimination score: calculated by time spent in social zone
764 minus time spent in empty zone/total time spent in both of these zones). **I-J.**
765 Quantification of time spent (**I**) and discrimination score (**J**) in second phase in three-

chamber test showing that decreased social interest with stranger after virus intervention (discrimination score: calculated by time spent in stranger zone minus time spent in original zone/total time spent in both of these zones). **K.** Different social interaction types in home cages increased after virus intervention of PV-Cre mice. **L.** Quantification of time spent showing that PV-Cre mice spent more time with social objects after virus intervention in home cage. **M-N.** Quantification of time spent showing that SST-Cre mice spent more time in the social zone before and after virus intervention (**M**) and discrimination score had no change of SST-Cre mice in three-chamber test of sociability stage (**N**). **O.** Traces of SST-Cre mice before (left) and after (right) virus intervention in the social preference test. **P-Q.** Quantification of time spent (**P**) and discrimination score (**Q**) in second phase in three-chamber test showing that SST-Cre mice spent more time in the stranger zone after virus intervention in three-chamber. **R.** Discrimination score showing that social interaction had no obviously change of SST-Cre mice spent with social object in home cage before and after virus intervention. Data are presented as the mean ± s.e.m. *p<0.05, **p<0.01, ***p<0.001, ****p<0.0001.

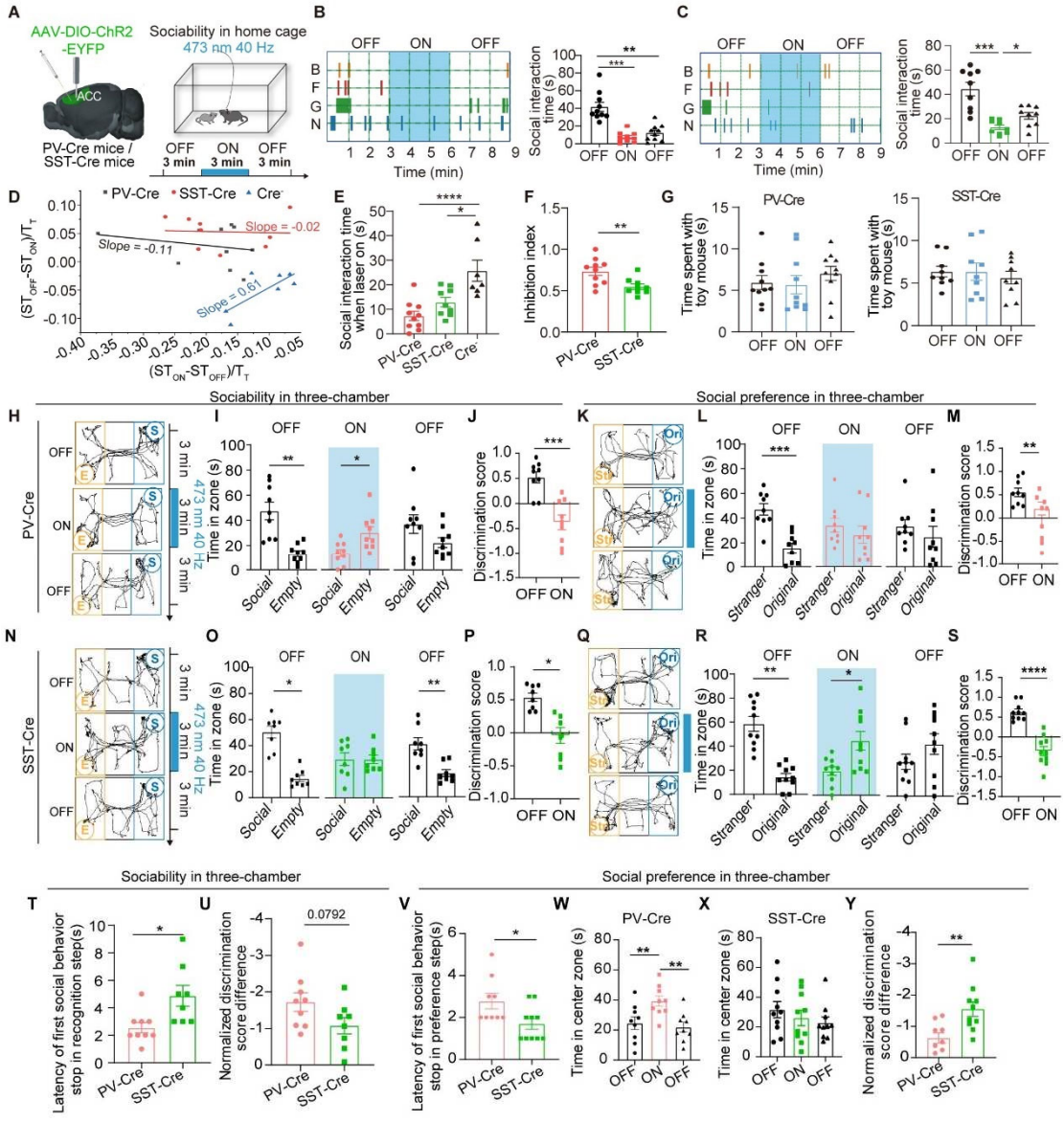

785

786 **Fig. 3 Optogenetic activation of PV or SST interneurons suppressed different**
787 **phases of social interactions. A.** Schematic of DIO-ChR2 injection into the ACC of
788 PV-Cre mice and SST-Cre mice (left) and diagram of the home cage test and laser
789 delivery strategy (right). **B.** Change process of different social interaction types in the
790 home cage when stimulus of PV-Cre mice (left) and statistical analysis of behavioral
791 changes in PV-Cre mice (right). **C.** The same as **B** but stimulus of SST-Cre mice. **D.**
792 Comparison of slope coefficient values in the PV-Cre group, SST-Cre group and EYFP
793 control group. **E.** Summary data of time of social interaction when laser on. **F.** Inhibition
794 index between PV-Cre mice and SST-Cre mice showing that the inhibition of PV-Cre

mice was more notable than that of SST-Cre mice (inhibition index: calculated by time spent with social object when laser off minus when laser on/total time spent with social object when laser off and on). **G.** Summary data of time spent with toy of PV-Cre mice group (left) and SST-Cre mice group (right). **H.** Traces of PV-Cre mice in the active social recognition test. **I.** Summary data of the active social recognition test showing that PV-Cre mice spent more time in the social zone (left panel) before laser on, spent more time in the empty zone when laser on (middle panel) and preferred the social zone after laser on (right panel). **J.** Discrimination score (calculated by time spent in the social zone minus time in the empty zone /total time spent in the social zone and in the empty zone) of PV-Cre mice in active social recognition. **K.** Traces of PV-Cre mice in the social preference test. **L.** Summary data of the social preference test showing that PV-Cre mice spent more time in the stranger zone (left panel) before laser on, no significant difference between the stranger zone and the original zone when laser on (middle panel) and after laser on (right panel). **M.** Discrimination score of PV-Cre mice in social preference test. **N.** Traces of SST-Cre mice in the active social recognition test. **O.** Summary data of the active social recognition test showing that SST-Cre mice spent more time in the social zone (left panel) before laser on, no time spending difference in social zone neither in empty zone when laser on (middle panel) and preferred the social zone after laser on (right panel). **P.** Discrimination score of SST-Cre mice in active social recognition. **Q.** Traces of SST-Cre mice in the social preference test. **R.** Summary data of the social preference test showing that SST-Cre mice spent more time in the stranger zone (left panel) before laser on, spent more time in the original zone when laser on (middle panel) and showed no significant difference after laser on (right panel). **S.** Discrimination score of SST-Cre mice in social preference test. **T.** Summary data of the delay time when the first social behavior stop of PV-Cre group and SST-Cre group in active social behavior in three-chamber. **U.** Comparison of discrimination scores between PV-Cre and SST-Cre mice in the active social test. **V.** Summary data of the delay time when the first social behavior stop of PV-Cre group and SST-Cre group in

stranger zone in three-chamber. **W-X.** Summary data of time spent in the center zone by PV-Cre mice (**W**) and SST-Cre mice (**X**) in the preference test. **Y.** Comparison of discrimination scores between PV-Cre and SST-Cre mice in social preference test. Data are presented as the mean ± s.e.m. *p<0.05, **p<0.01, ***p<0.001, ****p<0.0001.

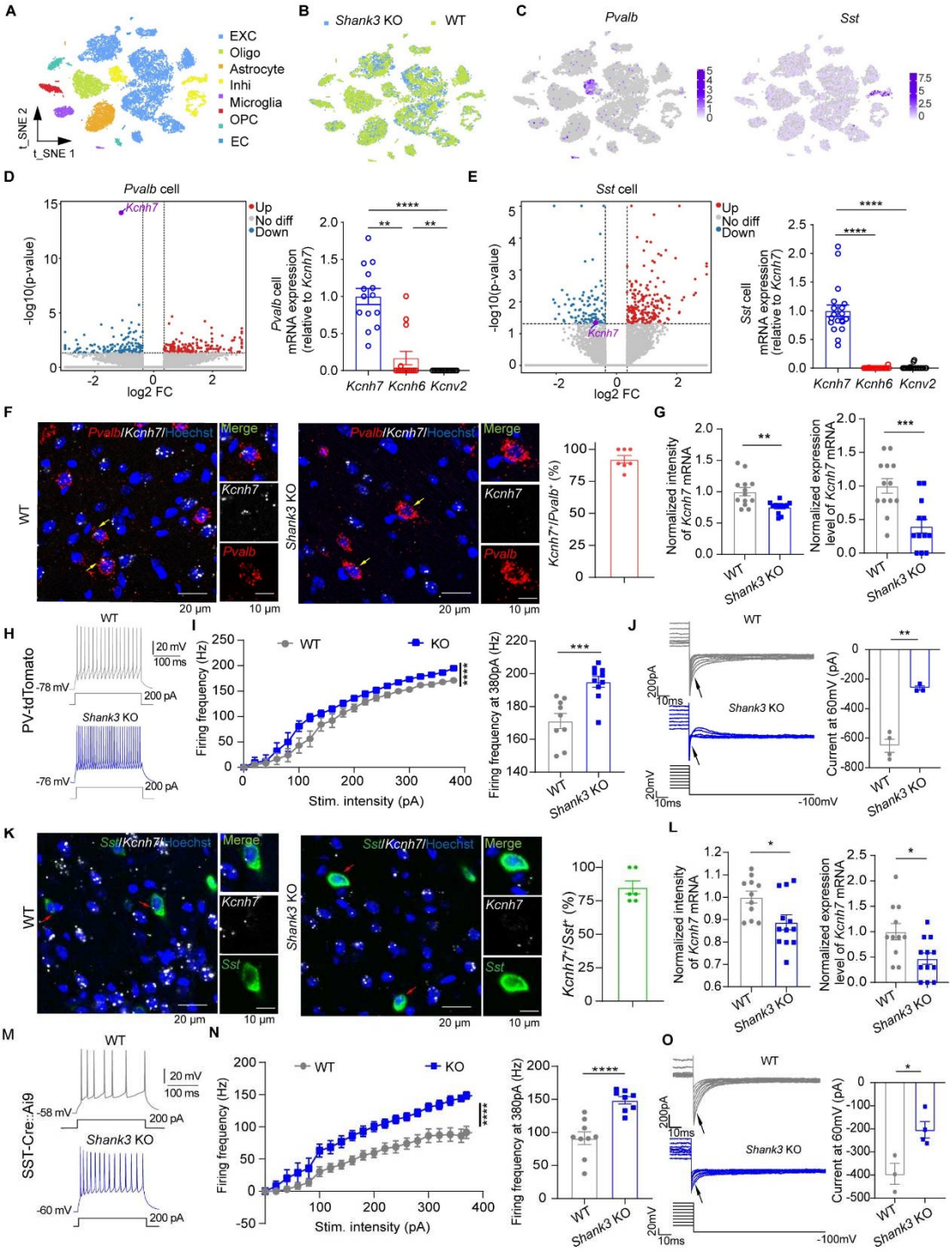

Fig. 4 Decreased levels of *Kcnh7* in PV and SST neurons within the ACC of *Shank3* KO mice resulted in heightened excitability in these interneuron subtypes. A-B. t-SNE plots of 17661 cells between the WT and *Shank3* KO groups (9391 cells in the WT group, 8270 cells in the KO group; one mouse per group). After alignment, cells allowing for a single joint clustering detected 7 populations. **C.** Feature plots showing single-cell gene expression of known markers for inhibitory neurons (*Pvalb*, left and

Sst, right). **D.** Volcano plot indicating upregulated and downregulated scRNA of *Pvalb* neurons between WT and KO mice (left). Relative mRNA expression of *Kcnh7*, *Kcnh6* and *Kcnv2* in *Pvalb* neurons (right). **E.** The same as **D** but for *Sst* neurons. **F.** Fluorescence images of FISH probing *Kcnh7* (gray) and *Pvalb* (red) images of *Kcnh7* expression on PV-positive neurons of WT mice (left) and *Shank3* KO mice (middle) and enumeration analysis of $Kcnh7^{+}/Pvalb^{+}$ (right). **G.** Normalized fluorescence intensity of *Kcnh7* mRNA (left) and normalized number of spots of *Kcnh7* mRNA (right) of $Pvalb^{+}$ neurons. **H.** Typical action potential trace at 200pA stimulus from PV-tdTomato mice in *ex vivo* recording between WT and KO mice. **I.** Input-output diagram of spike frequency at different stimulus intensities (left) and spike frequency at 380 pA stimulus intensity between WT and KO groups (right). **J.** Representative traces of ERG3 current between WT and KO groups (left) and the statistical results of the left (right). **K.** Fluorescence images of FISH probing *Kcnh7* (gray) and *Sst* (green) images of *Kcnh7* expression on SST-positive neurons of WT mice (left) and *Shank3* KO mice (middle) and enumeration analysis of $Kcnh7^{+}/Sst^{+}$ (right). **L.** Normalized fluorescence intensity of *Kcnh7* mRNA (left) and normalized number of spots of *Kcnh7* mRNA (right) for Sst^{+} neurons. **M.** The same as **H** but for SST-Cre::Ai9 neurons. **N.** The same as **I** but for SST-Cre::Ai9 neurons. **O.** The same as **J** but for SST-Cre::Ai9 neurons. Data are presented as the mean ± s.e.m. *p<0.05, **p<0.01, ***p<0.001, ****p<0.0001.

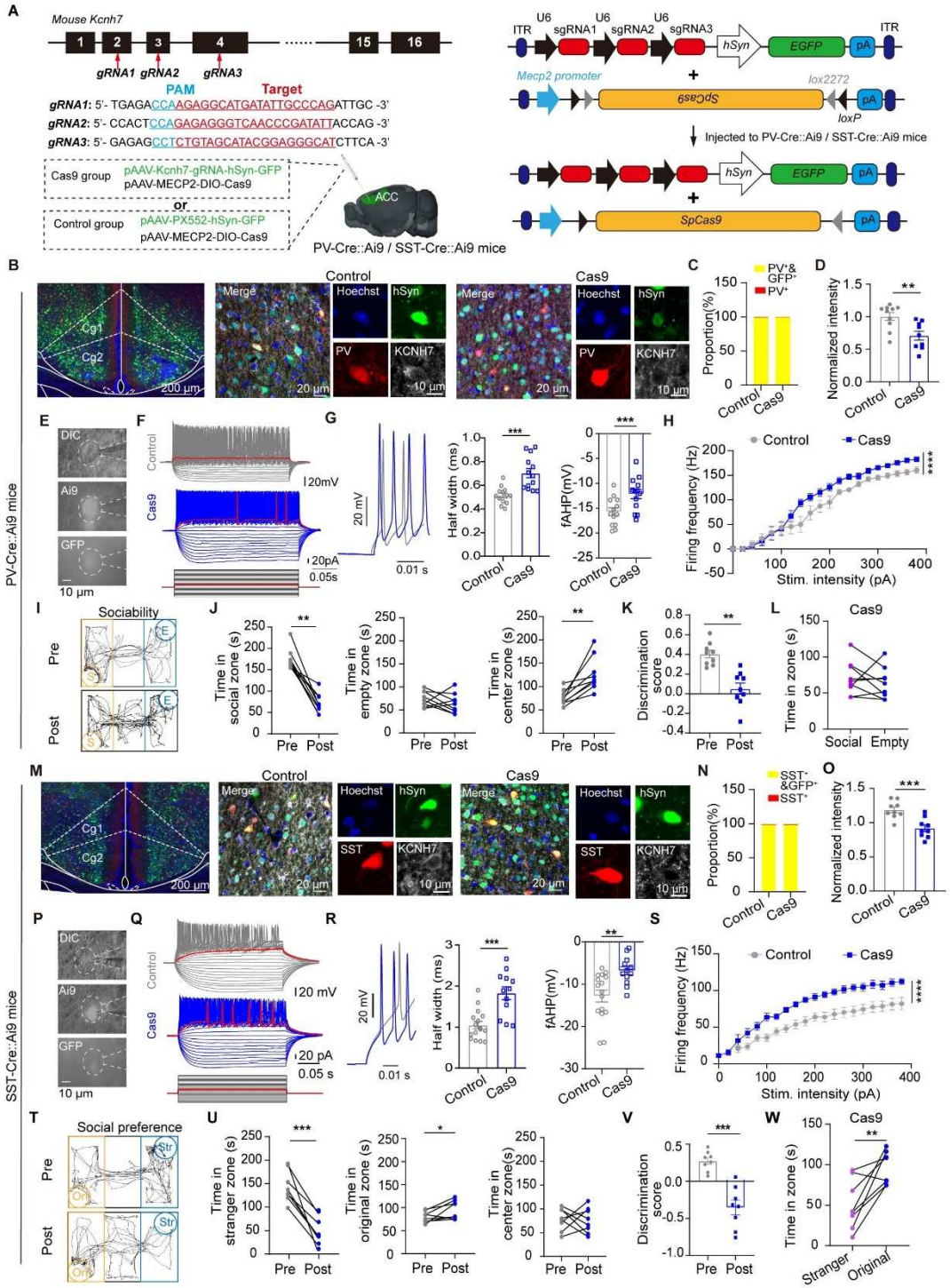

Fig. 5 Using CRISPR-Cas9 technology, specific KO *Kcnh7* in PV and SST neurons resulted in heightened neuronal excitability and differential impairment in social interaction. A. CRISPR-Cas9 viral approach to knockout *Kcnh7* in PV^+ neurons and SST^+ neurons. **B.** For PV-Cre mice, images showing AAV-sgRNA-hSyn-GFP expression (left) and KCNH7 expression between the control group (middle) and knockout group (right). **C-D.** More than 99% of PV^+ neurons were GFP^+ (**C**), and

relative KCNH7 protein expression significantly decreased after the CRISPR-Cas9 approach *in vivo* (**D**). **E-G.** *Ex vivo* recording from the control group and KO group (**E**) showing the neuronal excitability (**F**), action potential half width (**G** left, middle) and first after hyperpolarization (fAHP) (**G** right). **H.** Input-output diagram of spike frequency of PV-Cre neurons between control virus and Cas9 virus. **I-L.** Compared with social behavior prior to viral injection, PV-Cre mice spent less time in the social zone and more time in the center zone (**I-J**) and showed reduced sociability (**K-L**). **M.** For SST-Cre mice, images showing AAV-sgRNA-hSyn-GFP expression (left) and KCNH7 expression between the control group (middle) and knockout group (right). **N-O.** More than 99% of SST^+ neurons were GFP^+ (**N**), and relative KCNH7 protein expression significantly decreased after the CRISPR-Cas9 approach *in vivo* (**O**). **P-R.** *Ex vivo* recording from the control group and knockout group (**P**) showing the neuronal excitability (**Q**), action potential half width (**R** left, middle) and fAHP (**R** right). **S.** Input-output diagram of spike frequency of SST-Cre neurons between control virus and Cas9 virus. **T-W.** Compared with social preference behavior prior to viral injection, SST-Cre mice spent less time in the stranger zone and more time in the original zone (**T-U**) and showed reduced social preference (**V-W**). Data are presented as the mean ± s.e.m. *p<0.05, **p<0.01, ***p<0.001, ****p<0.0001.

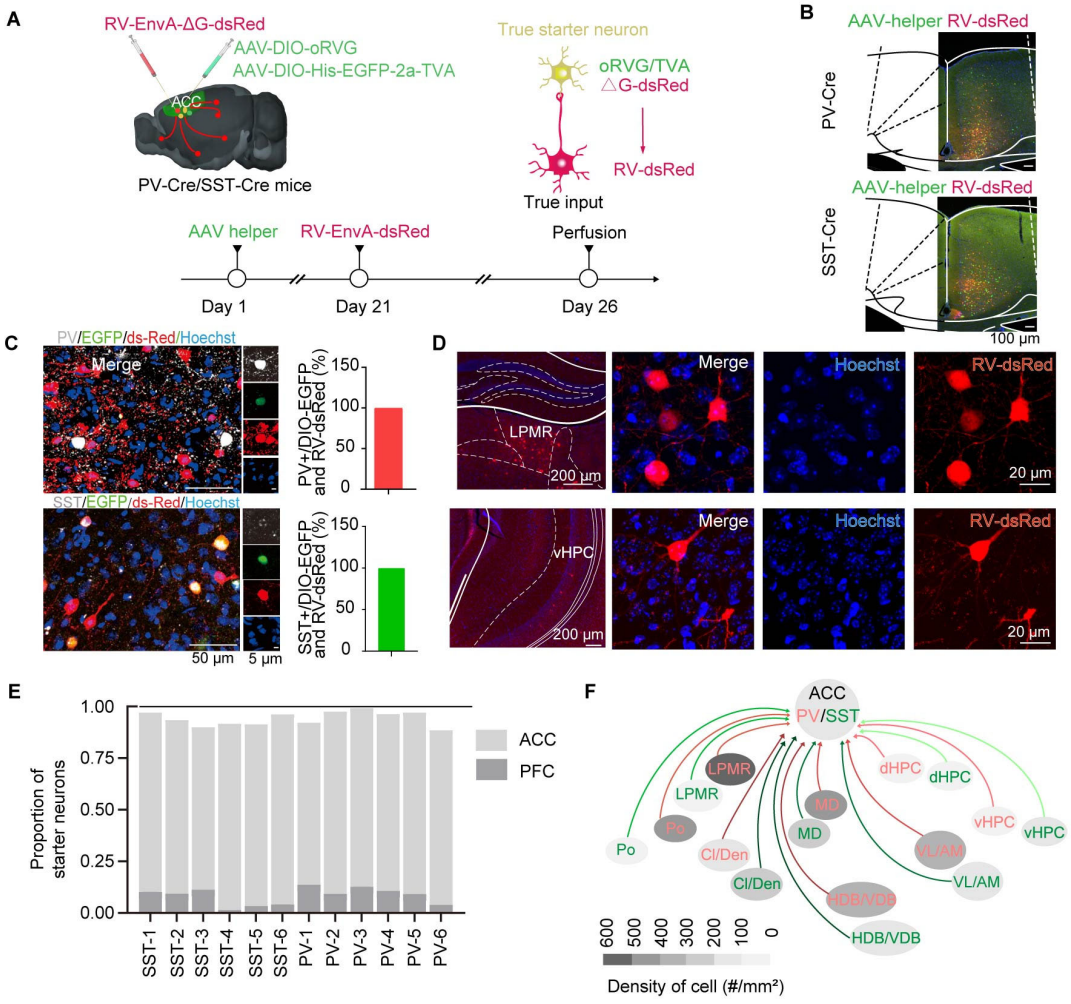

883

884 **Fig. 6 Retrograde monosynaptic tracing revealed that LPMR and vHPC may serve**
885 **as potential distinct inputs that innervate the PV and SST neurons within the ACC.**
886 **A.** The AAV helper virus was injected into the ACC of PV- and SST-Cre animals. Three
887 weeks later, RV-dsRed was targeted to the same location. Bicistronic expression of TVA
888 and oRVG from a single AAV vector optimizes the generation of true starter neurons,
889 that is, neurons able to give rise to retrograde transsynaptic labeling of monosynaptic
890 input neurons. Starter neurons are identified based on the coexpression of his-EGFP
891 and RV-dsRed. Input neurons only express RV-dsRed. **B.** AAV-hepler and RV-dsRed
892 expression in input neurons in representative sections of the ACC. **C.** Tracing of input
893 to ACC PV interneurons in PV-Cre animals (top) and tracing of input to ACC SST
894 interneurons in SST-Cre animals (bottom). Typical images indicate starter neurons in
895 the ACC coexpressing AAV-helper (his-EGFP, oRVG), RV-dsRed and PV or SST (gray).

D. PV neurons in the ACC receive direct inputs from the LPMR (top), and SST neurons in the ACC receive direct inputs from the vHPC (bottom). Images from a representative animal from each group. **E.** Targeting of the principal starter neurons (expressing his-EGFP and RV-dsRed) to the ACC subregions in the animals. 1.00 indicates all detected starter neurons. **F.** Analysis of the density of positive cells (RV-dsRed) in the upstream brain region. Data are presented as the mean ± s.e.m.

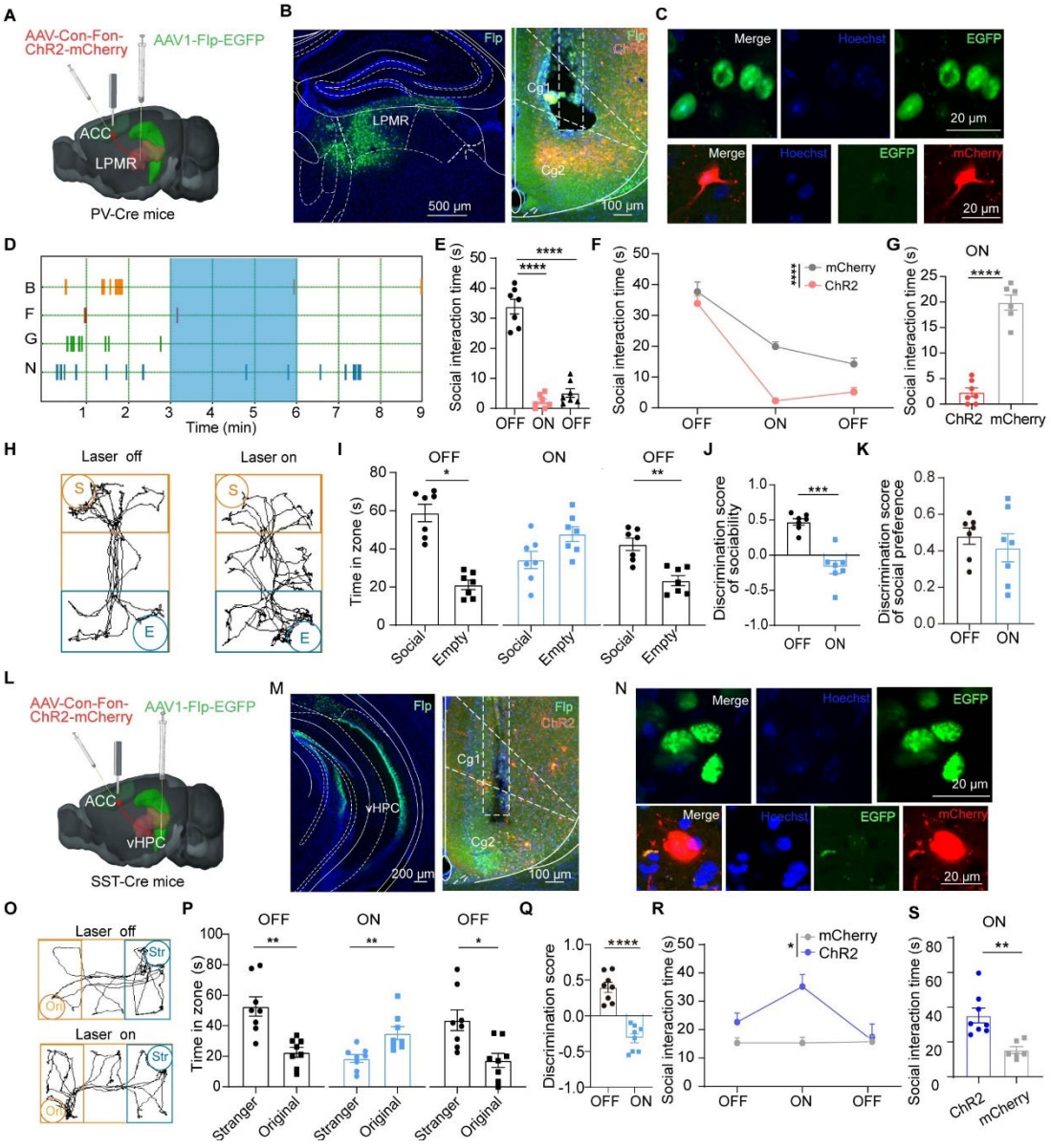

Fig. 7 Selective activation of the LPMR-PV (ACC) projection or vHPC-SST (ACC) projection produces distinct impairments in social interaction. A. Schematic of AAV1-Flp-EGFP injection into the LPMR and Con-Fon-ChR2-mCherry injection into the ACC of PV-Cre mice and optic fiber for laser embedding into the ACC. **B.** Representative micrograph showing the injection site in LPMR (left) and representative micrograph showing the site of optic fiber in ACC (right). **C.** AAV1 expression in LPMR (top) and AAV1-EGFP and ChR2-mCherry colabeled neurons in the ACC (bottom) of PV-Cre mice. **D-E.** Change process of different social interaction types in home cage when stimulus of PV-Cre mice (**D**) and quantification of social interaction

time in the home cage showing the effect of the laser on restraint of social time (**E**). **F-G.** Changes between the ChR2-mCherry and mCherry-control groups (**F**) and quantification of social time in **F** when laser on (**G**). **H.** Representative traces of sociability in the three-chamber of PV-Cre mice before laser on (left) and during laser on (right). **I.** Summary data of the active social recognition test showing that mice spent more time in the social zone (left panel) before laser on, no significant when laser on (middle panel) and preferred in the social zone after laser on (right panel). **J.** Discrimination score between laser off and laser on showing that activation of LPMR-PV (ACC) decreases active social interaction. **K.** Discrimination score between laser off and laser on showing that activation of vHPC-PV (ACC) has no influence on social preference. **L.** Schematic of AAV1-Flp-EGFP injection into the vHPC and Con-Fon-ChR2-mCherry injection into the ACC of SST-Cre mice and optic fiber for laser embedding into the ACC. **M.** Representative micrograph showing the injection site in the vHPC (left) and representative micrograph showing the site of optic fibers in the ACC (right). **N.** AAV1 expression in the vHPC (top) and AAV1-EGFP and ChR2-mCherry co-labeled neurons in the ACC (bottom) of SST-Cre mice. **O.** Representative traces of social preference in the three-chamber of SST-Cre mice before laser on (top) and during laser on (bottom). **P.** Summary data of the social preference test showing that mice spent more time in the stranger zone (left panel) before laser on, spent more time in the original zone when laser on (middle panel) and preferred the stranger zone after laser on (right panel). **Q.** Discrimination score between laser off and laser on showing that mice prefer social in original zone to in stranger zone when laser on. **R-S.** Change process between the ChR2-mCherry and mCherry-control groups in the original zone (**R**) and comparison of social interaction time between ChR2-mCherry and mCherry-control groups when laser on (**S**). Data are presented as the mean ± s.e.m. *p<0.05, **p<0.01, ***p<0.001, ****p<0.0001.

Methods

Mice. All experimental procedures were approved by the Institutional Animal Care and Use Committee (IACUC) of the Fourth Military Medical University (Approval No. IACUC-) and carried out according to the "Principles of Medical Laboratory Animal Care" issued by the National Ministry of Health in China. Adult (6–8 weeks old) male PV-Cre (Jax Stock no. 008069), SST-Cre (Jax Stock no. 013044), PV-tdtTomato (Jax Stock no. 027395), Ai9 (Jax Stock no. 007909), *Shank3B*$^{-/-}$[22] (Jax Stock no. 017688) and C57BL6 mice were used in this study. The animals were housed in a 12 h:12 h light–dark cycle (lights on at 8 AM) with food and water provided ad libitum. According to the double-blind principle, the experimenters were blinded to the experimental group.

Viral injections. *General procedure*. The mice were anesthetized with 1% pentobarbital sodium and placed in a stereotaxic instrument (RWD). Erythromycin eye ointment and a piece of silver paper were applied to prevent corneal drying. A thermostatic heating pad (ThermoStar, RWD) was placed under the body to keep the temperature constant during surgery. A small craniotomy hole was made using a dental drill (RWD), and injections were performed via a microsyringe pump (KD Scientific) at a flow rate of 40 nl/min to avoid potential damage to local brain tissue.

Optogenetics control behavior. AAV2/9-DIO-ChR2-EYFP was injected unilaterally into the ACC of PV-Cre or SST-Cre mice (virus titer: 3.2E+12 vg/mL, 240 nl/injection; AP: +0.73 mm; ML: -0.28 mm; DV: -1.75 mm, and optical fibers (2.5 mm optical density (OD), 0.37 numerical aperture (NA), 2.0 mm length) were implanted ipsilaterally.

Retrograde RV tracing of monosynaptic input of PV or SST interneurons to the ACC. A mixture of rAAV-EF1a-DIO-His-EGFP-T2A-TVA and rAAV-EF1a-DIO-oRVG (1:1 ratio, a total of 200 nl) was injected unilaterally into the ACC of PV-Cre or SST-Cre mice as a previous site to specifically infect monosynaptic input of PV interneurons or

SST interneurons. After three weeks, RV-EnvA-ΔG-dsRed was injected at the same coordinates. This viral strategy assures effective generation of RV and optimization of retrograde spread of RV-dsRed[86].

Functional verification of the projection loop. For synaptic tracing of LPMR to PV interneurons in the ACC and vHPC to SST interneurons in the ACC and confirmation of the role of projection, a mixture of rAAV2/1-Retro-ChR2 (5.08E+12 vg/mL) and rAAV-CAG-FLEX-GCaMP7s (2.21E+12 vg/mL) was injected into the ACC of PV-Cre and SST-Cre mice. Optical fibers were implanted in the ipsilateral LPMR (AP: -1.95 mm; ML: -1.64 mm; DV: -2.52 mm, 2.5 mm optical density (OD), 0.37 numerical aperture (NA), 3.0 mm length) or vHPC (AP: -3.2 mm; ML: -3.81 mm; DV: -1.57 mm, 2.5 mm optical density (OD), 0.37 numerical aperture (NA), 4.0 mm length) with 15° gradient and optical fibers (2.5 mm optical density (OD), 0.5 numerical aperture (NA), 2.5 mm length) were implanted ipsilaterally in ACC.

To confirm the function of these two projections *in vitro*, rAAV-hSyn-ChR2-mCherry (3.84 E+12 vg/mL) was injected into the LPMR or vHPC of PV-tdTomato or SST-Cre：：Ai9 mice.

Specific projection regulation. For specific regulation of LPMR→PV interneurons and vHPC→SST interneurons in the ACC, AAV1-Flp-EGFP (3.51 E+13 vg/mL) was injected into the LPMR (AP: -1.95 mm; ML: -0.85 mm; DV: -3.15 mm) of PV-Cre mice, and AAV1-Flp-EGFP was injected into the vHPC (AP: -3.2 mm; ML: -3.2 mm; DV: -2.8 mm) of SST-Cre mice. At the same time, rAAV-hSyn-Con-Fon-mCherry (5.56 E+12 vg/mL) was injected into the ACC of PV-Cre or SST-Cre mice, and optical fibers (2.5 mm optical density (OD), 0.37 numerical aperture (NA), 2.0 mm length) were implanted ipsilaterally.

Fiber photometry. Fiber photometry was used to record calcium signals using a commercialized fiber photometry system (Thinker Tech). rAAV-CAG-FLEX-GCaMP7s (2.21E+12 vg/mL) was injected unilaterally into the ACC of PV-Cre or SST-Cre mice as previously described, and optical fibers (2.5 mm optical density (OD), 0.5

numerical aperture (NA), 2.5 mm length) were implanted ipsilaterally. We used dental acrylic (Super Bond) to support the ceramic ferrule. Mice were individually housed and allowed to recover for at least 1 week. To record fluorescence signals, GCaMP7s fluorescence was detected through the optic fiber using a fiber photometry system (Thinker Tech). The values of fluorescence change ($\Delta F/F_0$) were calculated by calculating $(F - F_0)/F_0$. The MATLAB-based software provided by Thinker Tech Company was used to analyze the results.

Behavioral tests and *in vivo* optogenetic manipulations. For optical stimulation, during behavioral tests, the device connection process is described above[22]. Mice were connected to the patch cable, which was connected through a fiber-optic rotary joint allowing free rotation of the fiber and then allowed to recover from handling before the behavior test was initiated. In the excitatory photogenetic experiment, the test was divided into three 3 min epochs: laser stimulation off, on and off (OFF-ON-OFF epochs). Photoactivation of PV interneurons or SST interneurons in the ACC was induced by 40 Hz light trains with 5 ms pulses of blue light generated by a 473 nm laser.

Social interaction in the home cage. This procedure was carried out as previously described[22]. One week before the experiment, we grasped the test mice every day to perform adaptability training. Mice were allowed to explore the home cage freely for 3 min (habituation) before an unfamiliar juvenile male mouse (3 weeks old) was introduced into the cage. Measured social interaction behaviors included body sniffing, anogenital sniffing, face or nose contact and close following (<1 cm) initiated by the test mouse. All behaviors were video-recorded and analyzed using SMART v.3.0 software by experimenters who were blinded to the testing conditions.

Three-chamber test. This procedure was carried out as previously described[22]. The apparatus was made of black perspex and consisted of three identical chambers (30 cm × 45 cm × 20 cm). Two cylindrical grid cages were placed in the corners of the outer chambers, allowing free interaction (visual, olfactory, and auditory) between the test mouse and caged mouse. Before the test, the test animal was placed in the chamber for

10 min to habituate then isolated in the middle area to wait for the experiment to begin. For the sociability test, a novel juvenile male mouse was placed in a wire cage placed in one corner of the chamber, and another empty wire cage was placed in the opposite corner. For the social preference test, anther stranger juvenile male mouse was put into an empty cage, and then the experimental subject was allowed to explore freely in three chambers. The time spent in each chamber and the time spent in close proximity to the wire cages were analyzed using SMART v.3.0 software.

Olfactory test. Urine collection as previously describe[87]. The experiment was carried out in open field. Urine filter paper and saline filter paper were placed on opposite sides of the open field to record the movement of mice when laser off and laser on. The time spent in each corner were analyzed using SMART v.3.0 software.

Virus intervention social behavior experiments. Before AAV-taCasp3 injection, all PV-Cre and SST-Cre mice underwent a pre-experiment, including social interaction in the home cage and three-chamber test. After that, AAV-taCasp3 (2.03E+12 vg/mL) was injected into the ACC. After three weeks, a new round of social interaction experiments was conducted again. The time spent with unfamiliar juvenile male mice in the home cage and in three chambers in close proximity to the wire cages was analyzed using SMART v.3.0 software. These results were compared before and after virus injection.

Immunocytochemistry. All animals were anesthetized with 1% pentobarbital sodium and perfused intracardially with 0.9% saline followed by 4% paraformaldehyde. Then, the whole brain was removed and placed in 30% sucrose solution for 3 days. For PV interneurons or SST interneurons labeling, 40 μm cryostat sections containing the ACC were placed in blocking solution for 1 h before incubation in primary antibody against PV (rabbit, 1:100, Abcam, ab181086), primary antibody against SST (rat, 1:50, Millipore, MAB354), primary antibody against KCNH7 (rabbit, 1:50, Proteintech, 13622-1-AP), and primary antibody against NeuN (mouse, 1:500, Abcam, ab104224) overnight at room temperature. One hour after the behavior test, the whole brain samples were perfused, and these samples were stained for Fos (rabbit, 1:1500, CST,

#2250). Sections were then incubated with the corresponding secondary antibody at a dilution of 1:800 for 4 h at room temperature. Finally, all sections were incubated with Hoechst 33342 (Sigma) and were rinsed in 0.01 M PBS and cover-slipped with a mixture of 50% (v/v) glycerol in 0.01 M PBS.

VS200 continuous section scanning observation. After 7 days of injection with RV-EnvA-ΔG-dsRed, the animals were anesthetized with 1% pentobarbital sodium and perfused intracardially with 0.9% saline followed by 4% paraformaldehyde, and the whole brain was removed. After samples and sinking completely in 30% sucrose solution, the whole brain was cut into 40 μm sections on a cryotome (Leica). All sections were incubated with Hoechst 33342 (Sigma) and were rinsed in 0.01 M PBS and cover-slipped with a mixture of 50% (v/v) glycerol in 0.01 M PBS. Then, we used VS200 continuous section scanning (Olympus) to obtain images and counted the positive cells by OlyVIA (Olympus).

RNA extraction and quantitative real-time PCR. To verify the efficiency of AAV-taCasp3, we used a real-time PCR procedure to detect the mRNA levels of *parvalbumin* and *somatostatin* as previously described[88]. After the social behavior test, the mice were deeply anesthetized with isoflurane and sacrificed. The mouse skull was opened, and the whole brain was removed. Fresh ACC tissues were isolated from the corresponding coronal sections under a stereomicroscope. Total RNA was extracted with TRIzol reagent, and PrimeScript™ RT Master Mix (Takara) was used to reverse transcribe the total RNA (500 ng) into complementary DNA. Real-time PCR was carried out using a StepOnePlus™ Real-Time PCR Instrument (Thermo) with 2X Universal SYBR Green Fast qPCR Mix (ABclonal). The sequences of the primers used were as follows:

Target gene	F-	R-
GAPDH	GCGAGACCCCACTAACATCAA	GTGGTTCACACCCATCACAAA
Parvalbumin	GGGCCTGAAGAAAAAGAACC	TTCTTCAACCCCAATCTTGC
Somatostatin	ACCGGGAAACAGGAACTGG	TTGCTGGGTTCGAGTTGGC

Physiological recording from brain slices. *General procedure*. For brain slice preparation, the mice were deeply anesthetized withisoflurane, and coronal sections (300 μm thick) containing the ACC were cut using a vibratome (7000SMZ, Campden) in transcardially perfused with ice-cold carbogenated cutting solution containing 115 mM choline chloride, 2.5 mM KCl, 1.25 mM NaH_2PO_4, 0.5 mM $CaCl_2$, 8 mM $MgCl_2$, 26 mM $NaHCO_3$, 10 mM D-(+)-glucose, 0.1 mM L-ascorbic acid, and 0.4 mM sodium pyruvate (pH 7.4, with osmolarity of 295–300 mOsm/L). Then, brain slices were recovered for 30 min and incubated with carbogenated cutting solution (95% O_2, 5% CO_2) in a holding chamber at 32 ℃. After that, the brain slices were recovered for 1 h at room temperature in artificial cerebral spinal fluid (ACSF) (119 mM NaCl, 2.3 mM KCl, 1.0 mM NaH_2PO_4, 26 mM $NaHCO_3$, 11 mM D-(+)-glucose, 1.3 mM $MgCl_2$, and 2.5 mM $CaCl_2$ (pH 7.4, with osmolarity of 295–300 mOsm/L). After recovery, the slices were placed in the recording chamber and continuously perfused with ACSF. The recordings were obtained using a Multilamp 700B amplifier (Molecular Devices) filtered at 5 kHz and sampled at 20 kHz with a Digidata 1550B. Clampex 10.7 was used for acquisition and analysis.

Optical evoked spikes with ChR2. Patch pipettes were filled with a solution containing the following: 128 mM potassium gluconate,10 mM Na-phosphocreatine, 10 mM HEPES, 1.1 mM EGTA, 0.5 mM Na_2GTP, and 5 mM MgATP (pH 7.3, 300–305 mOsm/L). The cell membrane potential was clamped at −65 mV to record changes in spikes induced by ChR2 with 40 Hz stimulation.

Optical IPSCs. Patch pipettes were filled with a solution containing the following: 103 mM CsCl, 12 mM CsMeSO3, 12 mM CsOH, 12 mM methanesulfonic acid, 5 mM TEA-Cl, 10 mM HEPES, 4 mM MgATP, and 0.3 mM Na_2GTP (pH 7.3, 300–305 mOsm/L). Clamping the pyramidal neuron surrounded by fluorescence and the cell membrane potential was clamped at −65 mV and stimulated with ChR2-recording IPSCs in pyramidal neurons. 100 μM picrotoxin (PTX) was perfused verifying IPSCs property.

Intrinsic membrane properties. To measure the intrinsic membrane properties of PV interneurons and SST interneurons in the ACC, patch pipettes were filled with a solution containing as *Optical evoked spikes with ChR2.* Whole-cell recordings were carried out in current-clamp mode at −65 mV, and spikes were induced by incrementally increasing the current injection (each step increase was 20 pA).

Optical EPSCs. Patch pipettes were filled with a solution containing the following: 120 mM $CsMeSO_3$, 10 mM TEA-Cl, 5 mM NaCl, 10 mM HEPES, 4 mM MgATP, 0.3 mM Na_2GTP, 1.1 mM EGTA, and 4 mM lidocaine (pH 7.28, 295–300 mOsm/L). The laser intensity was adjusted to obtain a maximal response without overstimulation, and 0.5 ms blue light was applied with the cells clamped at −65 mV. Additional 1 μM tetrodotoxin (TTX) and 100 μM 4-AP were perfused followed by 20 μM NBQX to check whether the light-evoked PSCs were excitatory or inhibitory.

The excitability modulated by ERG3 channel. To observe the role of the ERG3 channel in active potential, 1-[2-(6-methyl-2-pyridyl)ethyl]-4-(4-methylsulfonylaminobenzoyl) piperidine (E-4031, Tocris), a blocker of ERG, was added to ACSF solution. Stock solutions of E-4031 (100 μM) were prepared in DMSO before dilution in ACSF; the final DMSO concentration never exceeded 0.1%, a concentration at which it did not affect the membrane potential and membrane currents.

Kv11 current recordings. For voltage-dependent K^+ current recordings, the low K^+ intracellular solution was composed of 55 mM potassium methanesulfonate, 5 mM KCl, 73 mM N-methyl-d-glucamine, 5 mM NaCl, 0.5 mM EGTA, 30 mM HEPES, 4 mM MgCl2, 4 mM MgATP and 0.4 mM Na_2GTP (pH 7.4, adjusted with HCl)[89]. For recording Kv11 currents from PV or SST-positive neurons in the ACC, 1 μM tetrodotoxin (TTX), 20 μM NBQX, 50 μM D-AP5 and 10 μM bicuculline were also supplemented in high K^+ intracellular solutions (10 mM KCl and no Ca^{2+}). These high K^+ extracellular and low K^+ intracellular solutions enable K^+ currents to be recorded as large, distinct inward currents. The signals were filtered at 3 kHz and digitized at 10 kHz in experiments for measuring Kv11 currents. The activation curve of the ERG

channels was extracted by dividing the peak amplitudes of E-4031-sensitive tail current traces at 0.5 ms after the voltage was changed to -100 mV.

scRNA-seq. *10X sample processing and cDNA library preparation.* From the fresh frozen mouse brain, two groups of ACC tissue were rapidly dissected from the cortex of *Shank3* KO and WT mice. Samples were homogenized in ice-cold homogenization buffer (0.25 M sucrose, 5 mM CaCl2, 3 mM MgAC2, 10 mM Tris-HCL pH 8.0, 0.1 mM EDTA, 1x protease inhibitor, and 1 U/μl ribolock RNase inhibitors) with a glass-on-glass dounce homogenizer prepared for extract nuclei. This process has been reported before[90].Nuclei concentration was adjusted to 1000 nuclei/μL and followed immediately by the 10X Genomics® Single Cell Protocol. Cellular suspensions were loaded on a 10X Genomics GemCode Single-cell instrument that generates single-cell Gel Bead-In-EMlusion (GEMs). Libraries were generated and sequenced from the cDNAs with Chromium Next GEM Single Cell 3' Reagent Kits v3.1. The cDNA libraries were sequenced on the Illumina sequencing platform by Genedenovo Biotechnology Co., Ltd (Guangzhou, China).

Sequencing and Cell Clustering. The Single Cell 3' Protocol produced Illumina-ready sequencing libraries. The cell-by-gene matrices for each sample were individually imported to Seurat version 3.1.1 for downstream analysis.

Differentially expressed gene analysis. The expression value of each gene in a given cluster was compared against the rest of the cells using the Wilcoxon rank sum test[91].

Fluorescent in situ hybridization. Mice were deeply anesthetized with isoflurane and transcardially perfused with 0.01 M PBS (pH: 7.4), followed by 4% paraformaldehyde in 0.01 M PBS. The brains were removed and fixed in 4% paraformaldehyde for 2 h and then put into 10%, 20%, 30% sucrose sequentially at 4°C until they sank to the bottom of the container. Frozen, 10 μm, coronal sections were cut on a cryostat (Leica). RNAscope in situ hybridizations were performed according to the manufacturer's instructions, using the RNAscope™ Multiplex Fluorescent Reagent Kit v2 for fixed-frozen tissue. Briefly, sections were dehydrated in sequential incubations with ethanol,

followed by 30 min Protease III treatment and washing in ddH_2O. Appropriate combinations of hybridization probes [here gene target name (mouse) and catalogue number: *Pvalb* 421931-C1, *Sst* 404631-C1 and *Kcnh7* 1007281-C2, ACD] were incubated for 2 h at 40 °C, followed by three amplification steps and incubated each channel with a specific color. Hoechst counterstaining and mounting with antifade mounting medium.

Single-cell qRT–PCR. Single PV-positive or SST-positive neurons in the ACC with red fluorescence signals were aspirated by a patch clamp. Each single cell was ejected into a tube with 5 μL of DPBS. Total RNA and cDNA from single neurons were isolated using a REPLI-g® WTA Single Cell kit (Qiagen) according to the manufacturer's instructions. qRT–PCR was performed with SYBR® Premix Ex Taq (ABclonal) in a CFX96 Touch Real-time PCR Detection System (Bio-Rad). Primer sequences are listed as follows:

Gapdh-Fp: 5′-AGGTCGGTGTGAACGGATTTG-3′,

Gapdh-Rp: 5′-TGTAGACCATGTAGTTGAGGTCA-3′;

Kcnh7-Fp: 5′-CCAGGAAACTGGACCGATACT-3′,

Kcnh7-Rp: 5′-CCAATCGCATACCAGATGCAA-3′;

Kcnh6-Fp: 5′-GACGTGCTTTCCACTCTCTAC-3′,

Kcnh6-Rp: 5′-GCGCTTGATTTGCCTGGTC-3′;

Kcnv2-Fp: 5′-ATGGTCCTTGAGCTACAAGCC-3′,

Kcnv2-Rp: 5′-CCCCGCAGTCCTCATCTTC-3′.

CRISPR-Cas9. *In vivo genome editing. In vivo* knockdown experiments targeting *Kcnh7* employed an AAV CRISPR/Cas9 approach. The single guide RNA (sgRNA) with high specificity and high efficiency were computationally identified from sgRNA libraries for genome-wide CRISPR knockout screening. Three U6-sgRNA (FE) gene fragments with the F+E tracrRNA backbone were synthesized by Integrated DNA Technologies (sequences are provided below, spacer sequences are capitalized). These fragments were cloned into the pX552-EGFP plasmid by In-Fusion Snap assembly

master mix (Takara 638948) to construct pX552-3xsgRNA(FE)-EGFP.

The AAV vectors were serotyped with PHP.eB coat proteins (3.64 x 10^13 genome copy (GC) ml-1 viral titers for). Briefly, sgRNA plasmids, pAdDeltaF6 (Addgene, plasmid #112867), and pUCmini-iCAP-PHP.eB (Addgene, plasmid #103005) were co-transfected into HEK293T cells using polyethylenimine (Cat. No. 23966, Polysciences). Cells were harvested 72 h post transfection by 5,000 x g centrifugation at 4°C for 10 min. Virus in media was precipitated by 8% PEG8000 (89510-1KG-F, Sigma). Cell pellets and virus precipitated from media were re-suspended in digestion buffer containing 500 mM NaCl, 40 mM Tris base, and 10mM $MgCl_2$. Benzo nuclease (10 KU, novoprotein) was added in the digestion buffer and incubated at 37 °C water bath for 1 hr. Next, we performed centrifugation at 2,000 x g for 10 min, and the supernatant was used on a discontinuous gradient of 15%, 25%, 40%, and 60% iodixanol in a 39 mL ultracentrifuge tube (No. 344326, Beckman). Ultracentrifugation was performed at 350,000 x g, 18°C for 2.5 hr. 5 mL fractions in 40% layer and 40%–60% interface was collected. These fractions were desalted using a 100 kDa cutoff ultrafiltration tube (15 ml, Millipore). Buffer was exchanged 4 times with 1x PBS with 0.001% Pluronic F-68. AAV titers were determined by real-time quantitative PCR (qPCR) using the primers of ITR. Forward primer: 5' GGAACCCCTAGTGATGGAGTT 3'; Reverse primer: 5' CGGCCTCAGTGAGCGA 3'.

U6-sgkcnh7-1(FE) sequence

gagggcctatttcccatgattccttcatatttgcatatacgatacaaggctgttagagagataattggaattaatttgactgtaaa
cacaaagatattagtacaaaatacgtgacgtagaaagtaataatttcttgggtagtttgcagttttaaaattatgttttaaaatgga
ctatcatatgcttaccgtaacttgaaagtatttcgatttcttggctttatatatcttgtggaaaggacgaaacaccgCTGGGC
AATATCATGCCTCTgtttaagagctatgctggaaacagcatagcaagtttaaataaggctagtccgttatcaactt
gaaaaagtggcaccgagtcggtgct

U6-sgkcnh7-2(FE) sequence

Aaggtcgggcaggaagagggcctatttcccatgattccttcatatttgcatatacgatacaaggctgttagagagataattag
aattaatttgactgtaaacacaaagatattagtacaaaatacgtgacgtagaaagtaataatttcttgggtagtttgcagttttaa

aattatgttttaaaatggactatcatatgcttaccgtaacttgaaagtatttcgatttcttggctttatatatcttgtggaaaggacga
aacaccGAATATCGGGTTGACCCTCTCgtttaagagctatgctggaaacagcatagcaagtttaaataag
gctagtccgttatcaacttgaaaaagtggcaccgagtcggtgct

U6-sgkcnh7-3(FE) sequence

Aaggtcgggcaggaagagggcctatttcccatgattccttcatatttgcatatacgatacaaggctgttagagagataattag
aattaatttgactgtaaacacaaagatattagtacaaaatacgtgacgtagaaagtaataatttcttgggtagtttgcagttttaa
aattatgttttaaaatggactatcatatgcttaccgtaacttgaaagtatttcgatttcttggctttatatatcttgtggaaaggacga
aacaccgATGCCCTCCGTATGCTACAGgttttagagctagaaatagcaagttaaaataaggctagtccgtt
atcaacttgaaaaagtggcaccgagtcggtgc

Statistical Analyses. All statistical analyses were performed in Prism 6.0 (GraphPad Software, Inc., USA). Values were expressed as the means ±s.e.m. Data were tested for significance using either an unpaired t test or a two-way repeated-measures ANOVA. Normally distributed data sets were analysed using a 2-tailed unpaired t test and 2-way repeated-measures ANOVA, followed by Tukey's multiple comparisons test. Data sets that were not normally distributed were analysed with a Kruskal-Wallis test with adjustments for multiple comparisons (**Extended Tables 1**). All behavioural, electrophysiological, biochemical and morphological data were obtained by counterbalancing experimental conditions with controls. Details of particular statistical analyses can be found in **Extended Tables 1**. Statistical significance was accepted when $p < 0.05$.

Data availability. The raw sequencing data of the scRNA-seq have been deposited in the Genome Sequence Archive in BIG Data Center (http://bigd.big.ac.cn/), Beijing Institute of Genomics (BIG), Chinses Academy of Sciences, under the accession number: **CRA013264**. The other datasets generated or analyzed during the present study are available from the corresponding author upon reasonable request.

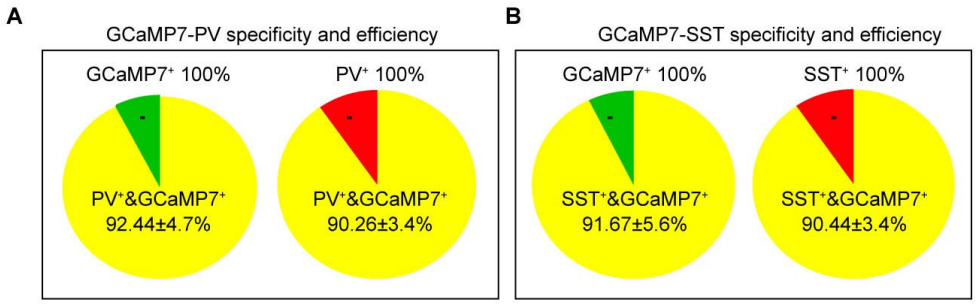

Extended Data Fig. 1 Validation of virus expression specificity in PV or SST neurons for GCaMP7. **A.** The percentage of PV^+ cells in $GCaMP7^+$ cells (left) and the percentage of $GCaMP7^+$ cells in PV^+ cells (right). **B.** The percentage of SST^+ cells in $GCaMP7^+$ cells (left) and the percentage of $GCaMP7^+$ cells in SST^+ cells (right). Data are presented as the mean ± s.e.m.

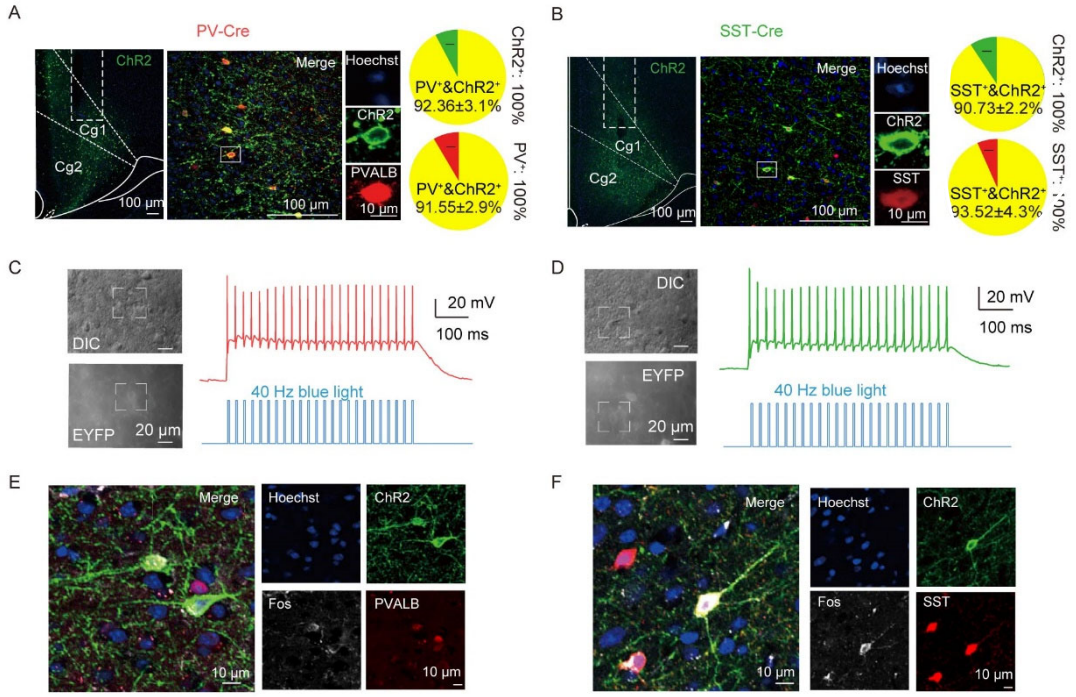

Extended Data Fig. 2 Verifying the expression of ChR2 in PV and SST neurons. A. Representative micrograph showing the placement of an optic fiber for optogenetics in the ACC of PV-Cre mouse injected with ChR2 and ChR2 expression in PV-positive interneurons (left). The pie charts showing the percentage of PV^+ cells in $ChR2^+$ cells and the percentage of $ChR2^+$ cells in PV^+ cells (right). **B.** Representative micrograph showing the placement of an optic fiber for optogenetics in the ACC of SST-Cre mouse injected with ChR2 and ChR2 expression in SST-positive interneurons (left). The pie charts showing the percentage of SST^+ cells in $ChR2^+$ cells and the percentage of $ChR2^+$ cells in SST^+ cells (right). **C.** Representative image of DIC (left) and representative trace evoked by a 40 Hz 473 nm laser (right) of PV-positive interneurons. **D.** Representative image of DIC (left) and representative trace evoked by a 40 Hz 473 nm laser (right) of SST-positive interneurons. **E.** Fos expression in PV/ChR2 co-labeled interneurons. **F.** Fos expression in SST/ChR2 co-labeled interneurons. Data are presented as the mean ± s.e.m.

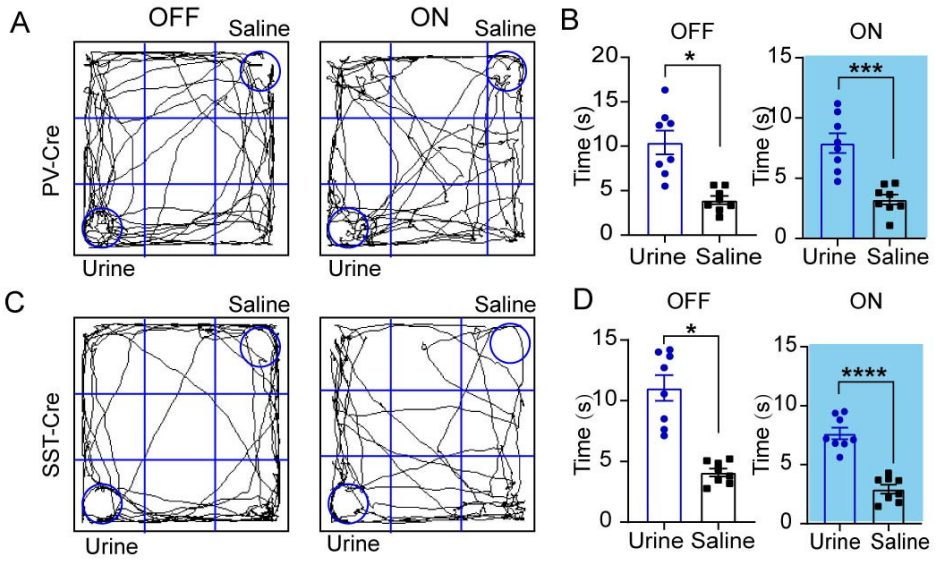

Extended Data Fig. 3 The activation of PV or SST interneurons did not alter the preference for urine induced by the unfamiliar mouse. A. Traces of PV-Cre mice when laser off (left) and when laser on (right) with urine and saline in each corner. **B.** Statistics of time in saline zone and urine zone in **A**. **C.** Traces of SST-Cre mice as **A**. **D.** Statistics of time in saline zone and urine zone in **C**. Data are presented as the mean ± s.e.m. *p<0.05, ***p<0.001, ****p<0.0001.

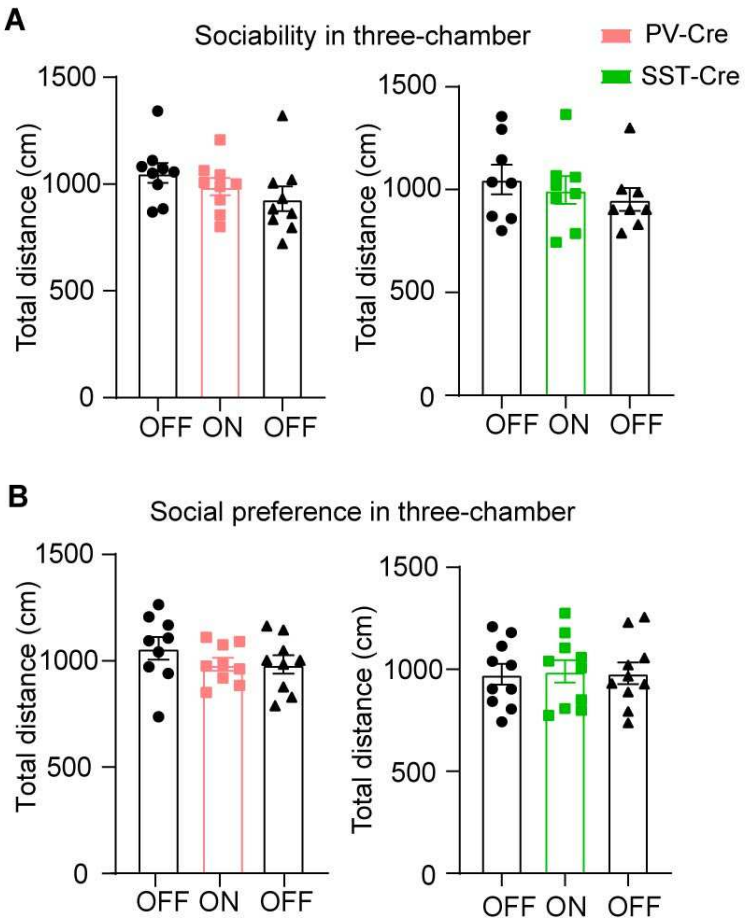

Extended Data Fig. 4 The activation of PV or SST interneurons did not result in any significant alteration in the total distance traveled by mice within the three-chamber. A. No changes in the total distance traveled by PV-Cre mice in the sociability test (left) and no changes in the total distance traveled by SST-Cre mice in the sociability test (right). **B.** No changes in the total distance traveled by PV-Cre mice in the social preference test (left) and no changes in the total distance traveled by SST-Cre mice in the social preference test (right). Data are presented as the mean ± s.e.m.

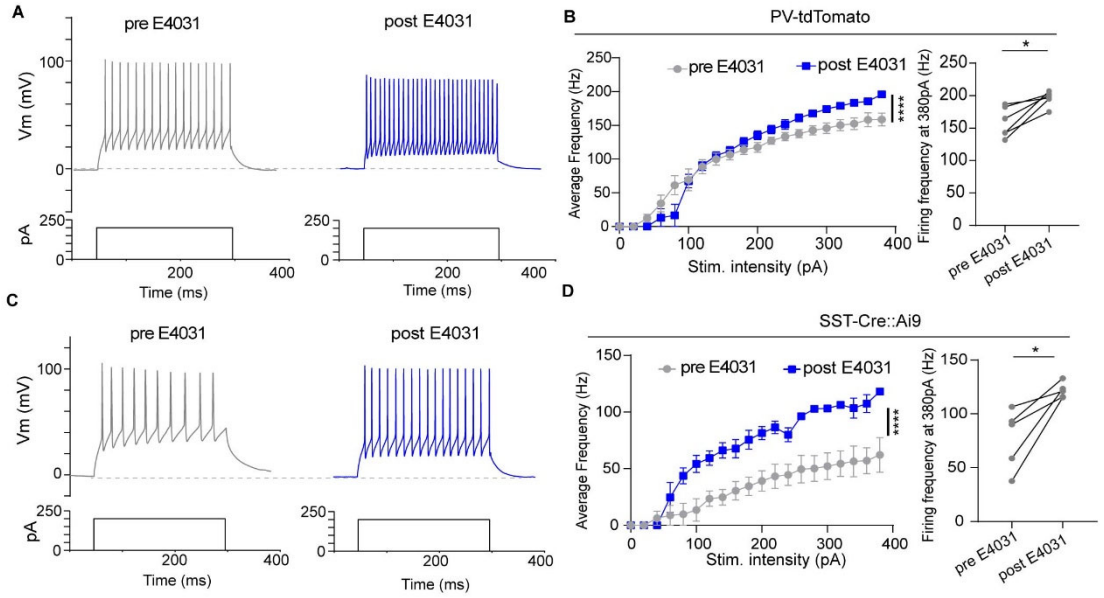

Extended Data Fig. 5 PV and SST neurons in ACC displayed increased excitability in the application of E-4031 *in vitro*. A. Spike trace of PV-tdTomato neurons before applicating E-4031 (left) and after applicating E-4031 (right). **B.** Comparison of spike frequency of different stimulus intensities (left) and the statistical results of frequency at 380 pA stimulus (right). **C.** The same as **A** but for SST-Cre::Ai9 neurons. **D.** The same as **B** but for SST-Cre::Ai9 neurons. Data are presented as the mean ± s.e.m. *p<0.05, ****p<0.0001.

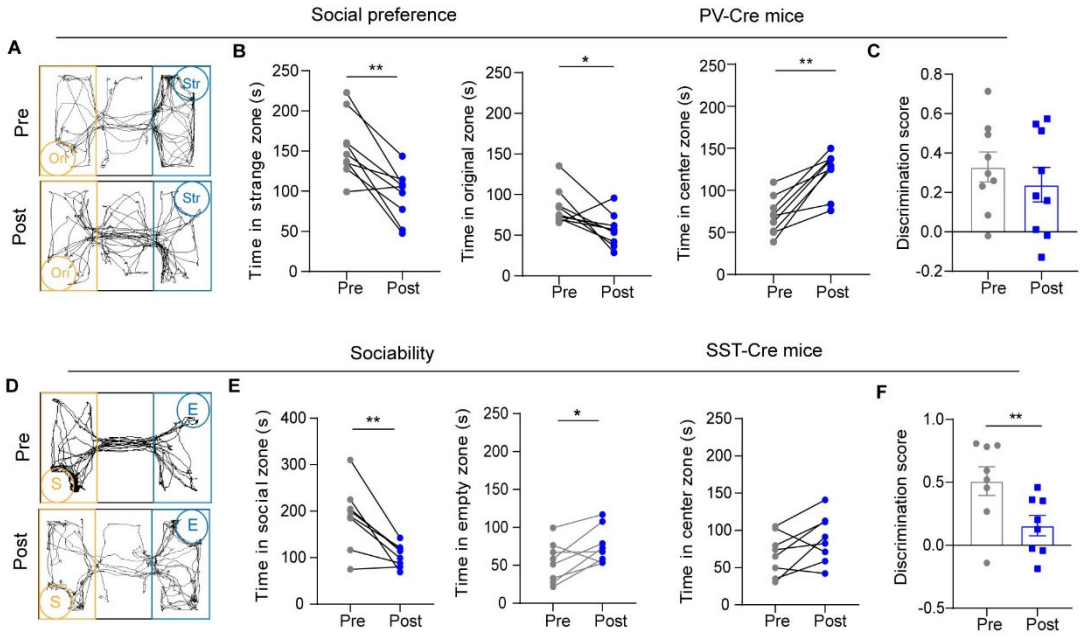

Extended Data Fig. 6 Specific KO of *Kcnh7* in PV or SST neurons did not change social preference or sociability following CRISPR-Cas9 intervention, respectively. **A-C.** Compared with social behavior prior to viral injection, PV-Cre mice spend less time in the stranger zone and original zone and spend more time in the center zone (**A-B**). Therefore, the social preference score does not change (**C**). **D-F.** Compared with social behavior prior to viral injection, SST-Cre mice spend less time in the social zone and spend more time in the empty zone (**D-E**) and display reduced sociability (**F**). Data are presented as the mean ± s.e.m. **p*<0.05, ***p*<0.01.

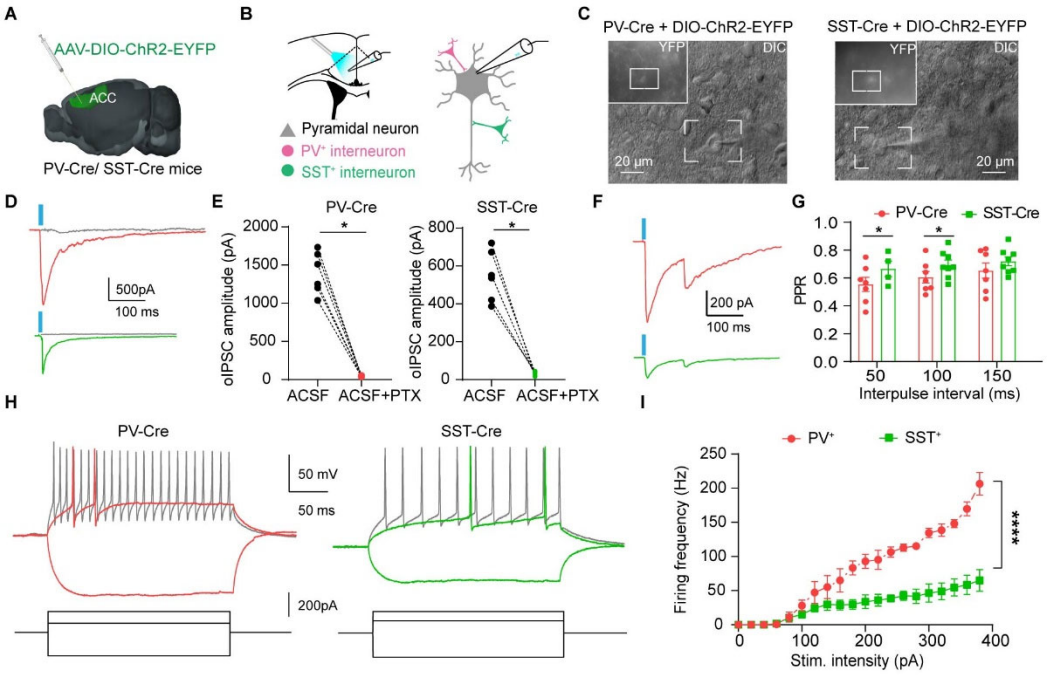

Extended Data Fig. 7 The PV and SST interneurons in the ACC have different electrophysiological characteristics. A. Schematic of DIO-ChR2 injection into the ACC of PV-Cre mice and SST-Cre mice. **B.** Schematic of recording IPSCs on pyramidal neurons by whole-cell recording. **C.** DIC display EYFP-labeled cells. **D.** IPSCs were induced by the laser on pyramidal neurons when stimulating PV interneurons (red) and could be blocked by PTX (gray, top); IPSCs were induced by the laser on pyramidal neurons when stimulating SST interneurons (green) and could be blocked by PTX (gray, bottom). **E.** Quantification of IPSC amplitude before and after PTX blocking in PV-Cre mice (left); quantification of IPSC amplitude before and after PTX blocking in SST-Cre mice (right). **F.** PPR traces induced by evoking PV interneurons (top) or SST interneurons (bottom). **G.** Quantification of PPR according to different stimulus intervals. **H.** Spike trace of PV interneurons (left) and SST interneurons (right). **I.** Comparison of spike frequency of different stimulus intensities between PV and SST interneurons. Data are presented as the mean ± s.e.m. *p<0.05, ****p<0.0001.

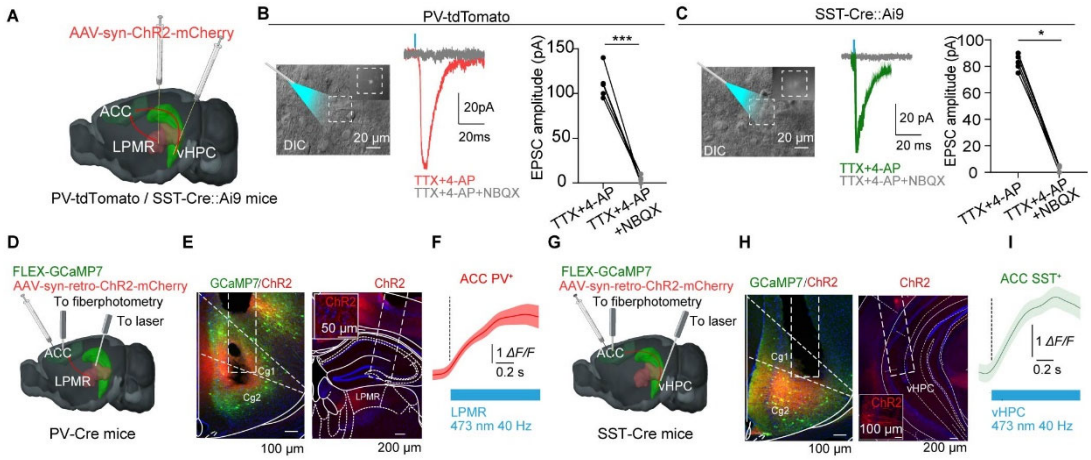

Extended Data Fig. 8 Both *in vitro* and *in vivo* results showed that the projections of LPMR to PV (ACC) and vHPC to SST (ACC) are glutamatergic. A. Schematic of syn-ChR2 injection into the ACC of PV-tdTomato mice and SST-Cre::Ai9 mice. **B.** Dotted frame indicating PV-tdTomato cells (left), 473 nm laser-induced EPSCs on PV-tdTomato cells (red) and blocked by NBQX (gray)(middle), and quantification of EPSC amplitude before and after NBQX blockade (right). **C.** Dotted frame indicating SST-Cre::Ai9 cells (left) and 473 nm laser-induced EPSCs on SST-Cre::Ai9 cells (green) and blocked by NBQX (gray), and quantification of EPSC amplitude before and after NBQX blockade (right). **D.** Schematic of injecting a mixture of retro-ChR2 and FLEX-GCaMP7s into the ACC of PV-Cre mice, optic fibers for laser embedding into the LPMR and optic fibers for fiber photometry embedding into the ACC. **E.** Representative micrograph showing the site of the optic fiber in the ACC (left); representative micrograph showing the site of the optic fiber in the LPMR and showing the expression of ChR2 (right). **F.** Typical Ca^{2+} signal trace induced by a 473 nm laser in PV-Cre mice. **G.** Schematic of injecting a mixture of retro-ChR2 and FLEX-GCaMP7s into the ACC of SST-Cre mice, optic fibers for laser embedding into the vHPC and optic fibers for fiber photometry embedding into the ACC. **H.** Representative micrograph showing the site of the optic fiber in the ACC (left); representative micrograph showing the site of the optic fiber in the vHPC and showing the expression of ChR2 (right). **I.** Typical Ca^{2+} signal trace induced by a 473 nm laser in SST-Cre mice.

Data are presented as the mean ± s.e.m. *p<0.05, ***p<0.001.

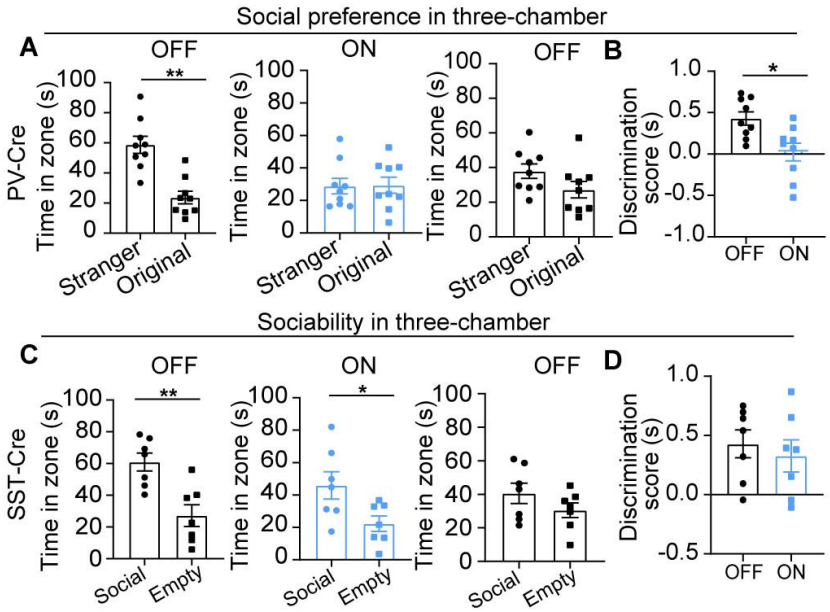

Extended Data Fig. 9 Specific activating LPMR-PV (ACC) projection or vHPC-SST (ACC) projection have no change on social preference or sociability, respectively. A. Summary data of the active social preference test showing that PV-Cre mice spent more time in the stranger zone (left panel) before laser on, no significant when laser on (middle panel) and no significant after laser on (right panel). **B.** Discrimination score between laser off and laser on showing that activation of LPMR-PV (ACC) decreases social time in the stranger zone. **C.** Summary data of the sociability test showing that SST-Cre mice spent more time in the social zone (left panel) before laser on and when laser on (middle panel) and no significant after laser on (right panel). **D.** Discrimination score between laser off and laser on showing no significant change in social time in the social zone and after activation of vHPC-SST (ACC). Data are presented as the mean ± s.e.m. *p<0.05, **p<0.01.

Supplementary Files

This is a list of supplementary files associated with this preprint. Click to download.

- ExtendedTables1.docx
- Extendedvideo1PVcresociability.mp4
- Extendedvideo2SSTcresocialpreference.mp4